MASARYKOVA UNIVERZITA
Přírodovědecká fakulta
Ústav teoretické fyziky a astrofyziky

Bakalářská práce

Brno 2023 Ema Šipková

MASARYKOVA
UNIVERZITA
PŘÍRODOVĚDECKÁ FAKULTA
ÚSTAV TEORETICKÉ FYZIKY A ASTROFYZIKY

Origin of TIC 229741985 variability

Bakalářská práce

Ema Šipková

Vedoucí práce: Mgr. Marek Skarka, Ph.D. **Brno 2023**

Bibliografický záznam

Autor:	Ema Šipková Přírodovědecká fakulta, Masarykova univerzita Ústav teoretické fyziky a astrofyziky
Název práce:	Mechanismus proměnnosti TIC 229741985
Studijní program:	PrF B-FY Fyzika
Studijní obor:	PrF ASTRO Astrofyzika
Vedoucí práce:	Mgr. Marek Skarka, Ph.D.
Akademický rok:	2022/2023
Počet stran:	xiii + 64
Klíčová slova:	Proměnné hvězdy, dvojhvězdy, pulzující hvězdy, δ Scuti, W UMa, TESS

Bibliographic Entry

Author:	Ema Šipková Faculty of Science, Masaryk University Department of theoretical physics and astrophysics
Title of Thesis:	Origin of TIC 229741985 variability
Degree Programme:	PrF B-FY Physics
Field of Study:	PrF ASTRO Astrophysics
Supervisor:	Mgr. Marek Skarka, Ph.D.
Academic Year:	2022/2023
Number of Pages:	xiii + 64
Keywords:	Variable stars, binary stars, pulsating stars, δ Scuti, W UMa, TESS

Abstrakt

Klasifikační systém proměnných hvězd rozlišuje mechanismy proměnnosti na základě podobnosti v chování jednotlivých objektů. U objektů, které vykazují charakteristiky více kategorií je problematické určit původ jejich proměnnosti a často jej lze odhalit pouze dodatečným pozorováním a podrobným zkoumáním. V této práci zkoumám TIC 229741985, abych odhalila mechanismus zodpovědný za pozorované světelné změny a popsala jeho parametry. Pozorovaná perioda světelných změn spadala do typického rozsahu δ Scuti pulzátorů; kdežto tvar světelné křivky fázovaný s dvojnásobnou periodou byl podobný světelným křivkám dvojhvězd typu W UMa. Zkoumám různé hypotézy popisující povahu těchto světelných změn pomocí fotometrických dat z mise *TESS*, vlastních fotometrických pozorování a spekter z Ondřejovského Echelletového Spektrografu, doplněných daty z nejrůznejších katalogů. Ověřuji možnost existence systému s těmito parametry, porovnávám výsledky se vztahy zjištěnými z předchozích pozorování proměnných hvězd typu δ Scuti a W UMa a diskutuji možný vliv třetího objektu ve dvojhvězdné soustavě. Ačkoliv výsledky stále nejsou jednoznačné, TIC 229741985 je s největší pravděpodobností pulzující hvězda typu δ Sct.

Abstract

The classification system of variable stars differentiates between mechanisms of variability based on similarities in the behavior of individual objects. Determining the origin of light variations is problematic for objects that exhibit characteristics of multiple categories and often can be resolved only by additional observations and detailed examination. In this thesis, I investigate TIC 229741985 to reveal the mechanism responsible for observed light variations and describe its parameters. The observed period of light variations fell within the range typical of δ Scuti pulsators; however, the shape of the light curve phased with double the period was similar to the W UMa binary. I investigate various hypotheses that describe the nature of these light changes with photometric data from the *TESS* mission, original photometric observations, and spectra from the Ondřejov Echelle Spectrograph, supplemented by catalog data. I verify the possibility of existence of a system with these parameters, compare the results with relations determined from previous observations of δ Scuti, and W UMa variables, and discuss the possible influence of a third object in a binary system. Although the results are still not conclusive, they favor the δ Scuti nature of TIC 229741985.

MUNI
SCI

MASARYKOVA UNIVERZITA
PŘÍRODOVĚDECKÁ FAKULTA
KOTLÁŘSKÁ 2, 611 37 BRNO
IČ: 00216224
DIČ: CZ00216224

ZADÁNÍ BAKALÁŘSKÉ PRÁCE

Akademický rok: 2022/2023

Ústav:	Ústav teoretické fyziky a astrofyziky
Studentka:	Ema Šipková
Program:	Fyzika
Specializace:	Astrofyzika

Ředitel *ústavu* PřF MU Vám ve smyslu Studijního a zkušebního řádu MU určuje bakalářskou práci s názvem:

Název práce:	Mechanismus proměnnosti TIC 229741985
Název práce anglicky:	Origin of TIC 229741985 variability
Jazyk závěrečné práce:	angličtina

Oficiální zadání:
Různé mechanismy proměnnosti hvězd mohou vyvolat změny jasnosti, které jsou jsou na podobných časových škálách a mají podobné amplitudy a tvar. Cílem práce je odhalit podstatu proměnosti objektu TIC 229741985 s využitím přesných fotometrických dat z družice TESS, dostupných informací v databázích, a vlastních měření.

Vedoucí práce:	Mgr. Marek Skarka, Ph.D.
Konzultant:	doc. RNDr. Miloslav Zejda, Ph.D.
Datum zadání práce:	22. 11. 2022
V Brně dne:	8. 12. 2022

Zadání bylo schváleno prostřednictvím IS MU.

Ema Šipková, 24. 11. 2022
Mgr. Marek Skarka, Ph.D., 1. 12. 2022
RNDr. Luboš Poláček, 8. 12. 2022

Poděkování

Především bych chtěla poděkovat vedoucímu mé práce Mgr. Marku Skarkovi, Ph.D. za podporu, neocenitelnou trpělivost a cenné rady při vypracovávání této práce. Především děkuji za všechny poskytnuté příležitosti a čas, který mi věnoval.

Dále bych ráda poděkovala pozorovatelům ze Stelárního oddělení Astronomického ústavu Akademie věd České Republiky v Ondřejově za pořízení spektroskopických dat a pomoc při jejich zpracování. Také bych chtěla poděkovat doc. RNDr. Miloslavovi Zejdovi, Ph.D. a Mgr. Václavovi Glosovi za čas, který si našli na zaškolení při práci s dalekohledy a pomoc při fotometrických měřeních na observatoři na Kraví Hoře a ve Vyškově.

Práce částečně vychází z dat pořízených Perkovým 2m dalekohledem v Astronomickém ústavu AV ČR v Ondřejově. Práce vznikla za podpory grantu MŠMT LTT-20015.

Nakonec bych také chtěla poděkovat své rodině a přátelům, kteří mi byli oporou během celého studia.

Prohlášení

Prohlašuji, že jsem svoji bakalářskou práci vypracovala samostatně pod vedením vedoucího práce s využitím informačních zdrojů, které jsou v práci citovány.

Brno 23. května 2023 . . . . . .

Ema Šipková

Contents

Introduction

The classification system of variable stars was founded to distinguish between different mechanisms of variability and group objects with similar behavior, where individual classes are characterized by the shape of their light curve, supplemented by additional information. However, determining the origin of light variations in a studied object is often not as straightforward as it might seem. The obtained data may show behavior that fits into multiple categories and can be resolved only by additional observations and detailed examination. The most interesting are the objects that seemingly fall outside the parameters determined for each class because they expand our understanding of these objects and challenge the theoretical models.

TIC 229741985 was first identified during a large-scale classification of A-F stars in the northern *TESS* continuous viewing zone by Skarka et al. (2022), but an unambiguous classification could not be made. When analyzing the time series data, the dominant frequency of light variations was identified at 11 c/d, a typical frequency of δ Scuti variables. However, when we phased the photometric observations with half the dominant frequency at 5.5 c/d, the obtained light curve had a shape typical of W UMa binary systems, with minima of similar depth and continuous light variations.

This study presents a detailed examination of available data for TIC 229741985 to determine the origin of its variability and explain its behavior. The photometric data were taken from the *TESS* mission and supplemented by original observations in different photometric filters at Kraví Hora and Vyškov observatories. Spectroscopic data were the product of the Ondřejov Echelle Spectrograph at the Astronomical Institute of Czech Academy of Science.

In chapter 1, I overview the information about various variable objects and provide details about their classification. This chapter focuses on the description of binary systems, the mechanics of their light variations, and the description of pulsation mechanisms for radial and non-radial pulsators. Chapter 2 introduces the object of interest and lists its parameters from the Gaia Archive and the TIC catalog. Chapter 3 presents comprehensive information about the photometric and spectroscopic data sources and the procedures necessary to process the collected data. Chapter 4 focuses on analyzing gathered data and investigating various hypotheses regarding the origin of TIC 229741985 light variations. Additional parameters are calculated to verify the possibility of such a system's existence and compared with relations derived from previous observations of W UMa and δ Scuti systems. Furthermore, this study discusses a possible third-light hypothesis.

Chapter 1

Variable Stars

Variable stars are objects that change their brightness over a period of time. Depending on their nature, these changes range from 10^{-3} to tens of magnitude. The time scales of these changes can also be different: from 10^{-4} s to the time needed for the star to reach its next evolutionary step (Mikulášek & Zejda 2013).

With the development of new and more precise observational techniques and the rising quality of instruments used for photometric observation, variable stars needed to be categorized by their behavior and the causes of their variability. The main defining factor was the shape of their light curve, later supplemented by data from spectral observations (lines present in their spectrum, changes in intensity, equivalent width and profile of spectral lines, and radial velocities).

Figure 1.1 shows the "Variability tree," which provides an overview of several different types of variable photometric phenomena among stars and other celestial objects.

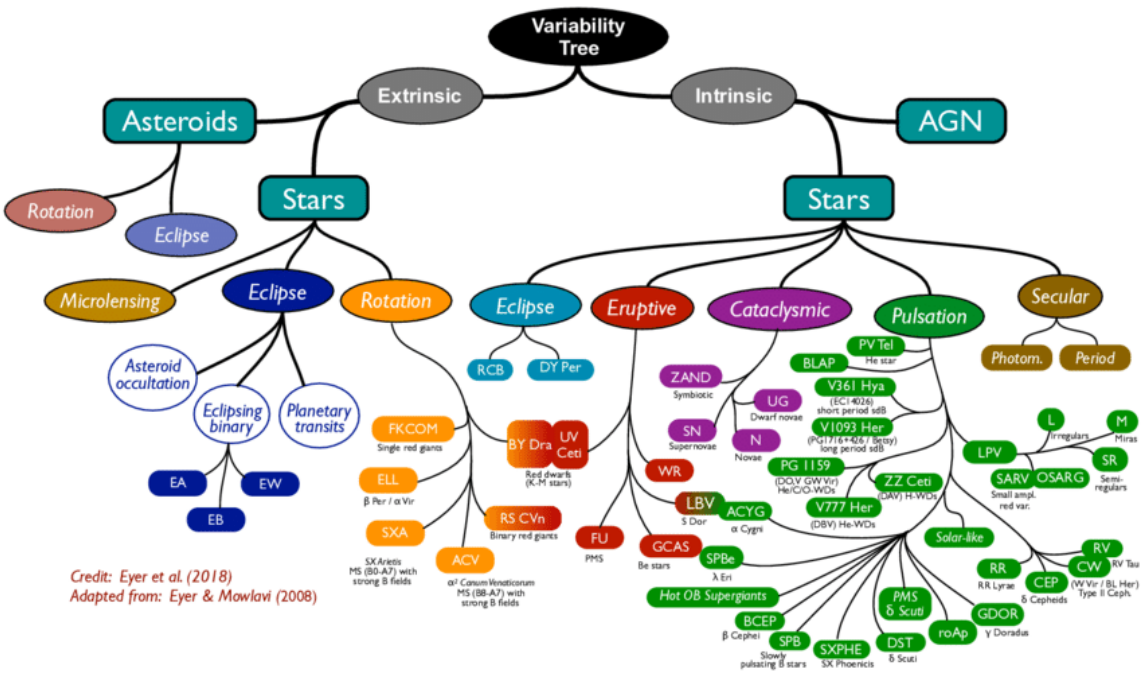

Figure 1.1: Stellar variability classification diagram (Gaia Collaboration et al. 2019).

According to the mechanisms of their variability, stars can be divided into two groups: intrinsic and extrinsic. This is the first level of division in the diagram in Fig. 1.1. The second level

comprises individual types of objects: stars, asteroids, and active galactic nuclei (AGN), further divided according to the phenomena responsible for their variability. The last level of division groups objects with similar characteristics or behavior (Eyer & Mowlavi 2008). Assigning the correct class to the specific star can be difficult, as some attributes of different classes may overlap, or the transition between them is continuous (Skarka et al. 2022).

Extrinsic variables

Extrinsic variables are objects whose irregularities in brightness are caused by external processes while their physical parameters remain unchanged. According to Catelan & Smith (2015), prototypical examples of this class are eclipsing stars, where the changes in brightness are caused by two or more bodies eclipsing one another in the observer's line of sight. Therefore, the system's geometry causes the object's variability.

Another example of a variable where the luminosity remains constant, but the observed brightness changes over time are the rotational variable stars. These stars have inhomogeneous temperatures across their surface, caused by cooler or hotter areas, e.g., starspots created by strong magnetic fields, faculae, etc. As the stars rotate, these areas enter or disappear from the observer's sight, leading to brightness fluctuations. Furthermore, stars do not have ideal spherical symmetry and can be deformed by their rotation. This leads to higher temperatures around the poles and variability of these objects if the rotational axis is subject to precession. Similar speculations can be made about asteroids - the change in the reflectivity across the surface leads to changes in their apparent brightness as the asteroid rotates.

Intrinsic variables

Intrinsic variable stars are divided into five categories, three of which I describe below. The other two categories are further discussed in the following sections. Most of these are connected with the evolution of stars or represent a stage in their lives.

- Stars with secular variations undergo slow and steady evolution, often characterized by long-term linear trends.
- Eruptive stars experience fluctuations in their brightness due to massive eruptions in their atmospheres. This subclass somewhat overlaps with subclasses of rotating variables because the eruptions in the chromosphere and coronae are associated with the interaction of magnetic fields on the star, as are the stellar spots and other phenomena. Flares of stellar energy and plasma can have life spans of various lengths. Among the effects characterizing different subclasses among eruptive stars also belong disk accretion and outflow (Catelan & Smith 2015).
- Cataclysmic variables contain the final stages of stellar evolution. The fate of a star depends solely on its mass. After the star burns through all available material, it finishes its life in one of two ways: it either remains an inactive object in hydrostatic equilibrium or explodes as a nova, supernova, or dwarf nova (Mikulášek & Krtička 2005). The star's collapse may continue even after the explosion, which leads to the creation of black holes.

Fig. 1.2 shows the positions of different types of variable stars against a reference sample (grey stars in the background) on color-magnitude diagrams. The top diagram shows different characteristics for individual types of pulsating stars in selected regions of the plot. In contrast, the bottom diagram shows that the eclipsing binaries can be found almost anywhere on the plot.

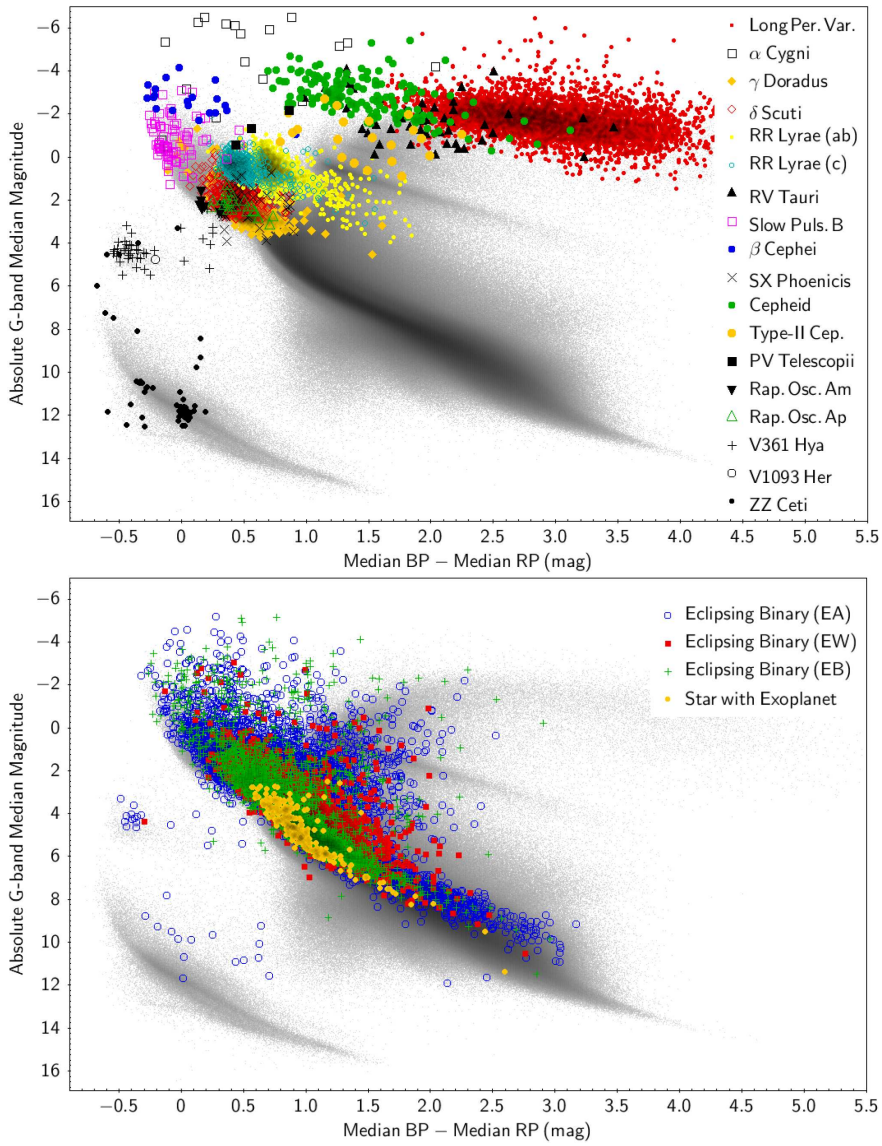

Figure 1.2: Positions of different types of variable stars on color-magnitude diagrams from Gaia Collaboration et al. (2019).

1.1 Binary Stars

Binary stars are systems where two stellar bodies orbit each other around their common center of mass. According to the various methods of observation, binary stars can be divided into four main groups (CSIRO n.d.):

- **Visual binaries** are systems where both components are observed near each other in the sky. Stars may be projected next to each other during observation but may not be gravitationally bound and have various distances from the observer. In that case, we refer to them as optical binaries. Astrometrical or spectroscopical observations can resolve this problem.

- **Astrometric binaries** were discovered by observing a spiral-like perturbation in their proper motions, indicating the presence of a second, often invisible component.

- **Spectroscopic binaries** were discovered by studying the shift of spectral lines in the detected spectrum. These systems cannot be visually observed as separate stars, but the presence of a second companion is indicated by the periodically changing wavelength of spectral lines. The period of these changes is the same as the orbital period of the system (Kamilla et al. 2011).

- **Eclipsing binaries** are mainly detected through photometric measurements. Fluctuations in their brightness are coincidental with eclipses of the components in the observer's line of sight.

Binary stars are gravitationally bound. All points that have the same potential are called equipotential surfaces. In a binary system, this potential is calculated as a sum of gravitational potentials from both components and an element that belongs to the centrifugal force in the given position. The shape of equipotential surfaces (Hill surfaces) depends on the mass ratio of binary components. Hill surface that passes through a Lagrangian point L_1 defines the shape of the Roche lobe. It is a boundary that defines space, where one component's gravitational effect outweighs the other component's gravitational influence (Mikulášek & Zejda 2013).

Stars take the shape of their equipotential surfaces. Single stars often have spherical equipotentials; therefore, their shape is spherical. Close binary stars are deformed into a teardrop shape by the other component. Kopal (1955) defined three categories of close binary systems based on how they fill out their Roche lobes: detached, semi-detached, and contact (overcontact) systems.

Detached binaries are systems where the volumes of both components are smaller than the volume of their Roche lobes. The typical representatives of this category are Algol type I variables. Their light curves have sharp and narrow primary minima and shallower but distinctive secondary minima caused by eclipses of the components. Brightness between the minima is almost constant; slight variations are linked with the ellipsoidal shape of the components or the reflection effect. Fig. 1.3 shows examples of detached eclipsing binaries' light curves.

Semi-detached systems refer to systems where only one of the components fills its Roche lobe. Algol type II stars are semi-detached systems typically with periods of several days with continuous light variations outside of their eclipses caused by the teardrop shape of one of its components. Typical for these binaries are the mass transfer from the larger star through the lagrangian point L1 and angular momentum loss. Example light curves of these systems are shown in Fig. 1.3.

Contact (Overcontact) binaries are systems where both stars fill out or exceed their Roche lobes. The components share a common envelope. Tidal forces from the second component and mass transfer deform close interacting binary systems. Among the effects in play are also disc accretion and reflection effects, where the light from one component reflects off the surface of the second component. This radiation is partly absorbed by the photosphere facing the first component, leading to a rise in temperature. The mass transfer also plays a vital role in their evolution; it speeds up the development of the less massive star.

W Ursae Majoris (W UMa) is a close or overcontact binary system with a shared envelope around both components. Because of this, stars in a W UMa system have the same surface temperatures and are of a similar spectral type. Orbital periods of these binary systems are relatively short, ranging from 0.25 to 1.0 days. Light curves show similar minima and continuous light variations because of the components' equal size and temperature (Malatesta n.d.). Examples of overcontact binaries' light curves are shown in the last two lines in Fig. 1.3.

In the first approximation, the motion of stars can be analytically solved as a two-body problem (Verbunt 2015). We can determine the masses of stars, orbital period, or system separation by applying Kepler's laws to a binary star system. In practice, the observations of trajectories are mostly relative because most systems do not have distinguishable components (Mikulášek & Krtička

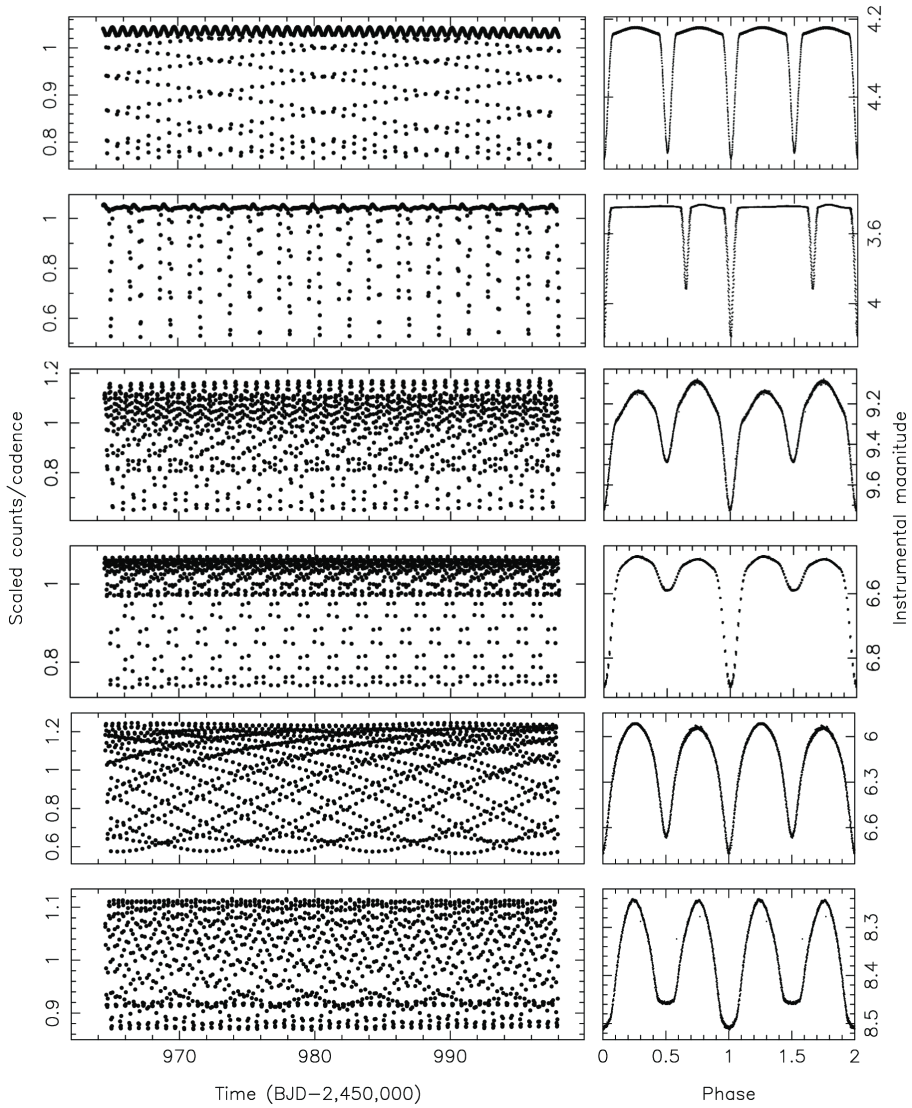

Figure 1.3: Example light curves of detached binaries (the two top diagrams), semi-detached binary systems (the two middle diagrams), and contact binary systems (the two bottom diagrams) (Prša et al. 2011).

2005). The fainter component orbits around the stationary brighter star on a relative ellipsoidal trajectory. The orbital period P can be determined from Kepler's third law:

$$P^2 = \frac{4\pi^2}{\mathrm{G}(M_1 + M_2)} a^3, \tag{1.1}$$

where G is a gravitational constant, M_1, M_2 are masses of the stars, and major axis a is given as a sum of their respective major axes. The study of eclipsing binaries makes it possible to determine stars' radii and masses.

Eclipses of binary stars cause changes in the observed light curves. According to Mikulášek & Zejda (2013), for an eclipse to occur, the system's inclination (an angle between the observer's line of sight and the normal vector to the orbital plane) has to be $i > 90° - \alpha$. The angle α is defined as

$$\sin\alpha = \frac{R_1 + R_2}{r}, \tag{1.2}$$

where R_1 and R_2 are the radii of the stars, and r is the radius of their circular trajectory around a common center of mass. If the smaller star passes through the center of the disc of its larger companion, the inclination is equal to 90°.

Light curves reflect the characteristics of studied systems, and many parameters affect their shapes. Light curves with similar characteristics often belong to the stars of a particular type.

1.2 Pulsating Stars

Changes in the surface characteristics caused by stellar pulsations are relatively stable phenomena that induce brightness variations. Changes in the star's radius generate radial pulsations, whereas nonradial pulsations result from changes in a star's shape. The energy needed for each pulsation cycle is fed through various driving mechanisms. Without this dotation, pulsations in the star would be damped by internal friction. Four known pulsation mechanisms are κ-mechanism, stochastic mechanism, ε-mechanism and γ-mechanism.

Within a star with pulsations driven by κ-mechanism exists a region where the material does not lose heat during compression and instead accumulates enough energy to sustain oscillations in the entire volume. This is not standard behavior for the stellar matter. It is only possible in the region with partially ionized hydrogen and helium, where the material's opacity blocks radiation and prompts the region's expansion beyond its equilibrium point. The ionized gas then reduces the opacity and becomes more transparent to radiation, which causes the region to contract again and the elements to recombine. Hydrogen and helium absorb energy during recombination, and the layer gains heat (Kurtz 2006). The effectivity of the κ-mechanism depends on the position of the ionized layer inside the star; if the region lies too close to the core, the amplitude of pulsations is negligible. On the other hand, if it lies too close to the star's surface, it cannot accumulate enough energy because the mass and density of the layer are insufficient (Mikulášek & Zejda 2013). For classical pulsators, radial pulsations appear during the evolutionary stage, when the star crosses across a region of an H-R diagram called the instability strip. It is a narrow band defined by stars of different effective temperatures that can maintain radial pulsations in their volume. Different pulsating stars are distinguished according to their mean density, connected to their position inside the strip.

The κ-mechanism is reinforced by processes that supply the compressed layer with heat because of the higher temperatures in the adjacent partially ionized layers, prompting further ionization. Increasing thermal capacities c_p and c_v cause the compressed layer to absorb more heat. This effect is called the γ-mechanism.

The stochastic mechanism is described as a mechanism that converts energy from the stochastic noise because the star resonates in some of its oscillation frequencies. This mechanism is a driving force for solar-like pulsators and red giants (Kurtz 2006).

Variations in energy generation in the star's core can supply the stellar pulsations. This type of driving mechanism is believed to be possible in massive stars and is known as the ε-mechanism.

When an object deviates from its equilibrium point, a restoring force appears, which tries to bring it back into balance. Stellar oscillations can also be divided into two groups according to the primary restoring force responsible for the pulsations:

- **Pressure modes** (p-modes) are acoustic waves, where the restoring force is pressure.
- **Gravity modes** (g-modes) have buoyance as the primary restoring force.

To understand the p-modes in a star, we can describe the behavior of sound waves in a pipe with one end closed and one open. At the closed end of the pipe, the sound wave always has a displacement node, and at the open end, a displacement antinode. Individual modes' frequencies depend on the environment's characteristics, primarily the pipe's length, air temperature, and chemical composition. If the individual overtones have small integer ratios with the fundamental frequency, we refer to them as harmonics.

When describing the p-modes, we can think of a star as a three-dimensional oscillator with a displacement node in the star's center and a displacement antinode on its surface. The oscillation modes can be described with three quantum numbers representing directions in a spherical coordinate system: n is called an overtone of the mode and refers to the number of radial nodes, l refers to the number of surface nodes and is called a degree of the mode, and m is the azimuthal order, describing the number of surface nodes along the longitude.

Radial pulsations are analogous to the oscillations in the half-enclosed pipe, while the non-radial quantum numbers are equal to zero. In the fundamental mode $n = 0$, the star expands and contracts with only one node located in the star's center. The first overtone has one additional node inside the star; the second overtone has two, etc. The sphere that defines the node is static, and the material below and above it moves in an antiphase. Overtones in the stars are not harmonic because the temperature and the chemical composition gradually change with the distance from the core, changing the speed of the sound in the material.

Nonradial modes are symmetric along the star's rotational axis, except for rapidly oscillating Ap stars, which are symmetric along the axis connecting its magnetic poles. They can exist only for $n \geq 1$. The simplest nonradial mode, where the star's equator is a node, and its hemispheres move in an antiphase, has $l = 1$ and $m = 0$. The center of mass for a star is not displaced during these oscillations. The m-modes are described as waves moving against the direction of rotation (retrograde modes) or waves traveling in the direction of its rotation (prograde modes).

Stars can pulsate in a combination of different modes; for example, the fundamental mode is the strongest in RR Lyrae stars and cepheids. In which mode the star pulsates is determined by its characteristics; chemical composition, magnetic field, the depth of the ionization zone, evolutionary stage, and many more. Asteroseismology studies the properties of the inner parts of stellar objects by determining their pulsation modes (Kurtz 2006).

According to the Stefan-Boltzmann relation, the luminosity of a star is tied to its temperature. As the star or its region expands due to pulsation, the surface temperature measured by an observer decreases, changing the star's observed brightness.

Stellar objects inside the instability strip with similar temperatures but different luminosity vary in density. The period of pulsations is related to the object's absolute magnitude because the periods of fundamental modes are closely related to the density inside the star and the position of the ionized layer.

Pulsating stars are divided into many subcategories according to their periods, amplitudes of light variations, and the shape of their light curves. One of the hypotheses for an object studied in this work describes it as a δ Scuti pulsator; therefore, I will only detail the characteristics of this subgroup.

δ Scuti

δ Scuti stars are a subgroup of pulsating stars located in an instability strip near the main sequence. They are radial and nonradial pulsators with spectral types A0 to F0 with relatively short periods ranging from 0.01 to 0.2 days. Their lightcurves depend on their pulsation mode; if the star oscillates in several different modes, its lightcurve changes amplitude and shape. Pulsations in different modes can cancel each other out or strengthen themselves, changing the amplitude of their

light variations. Fig. 1.4 shows several light curves of δ Scuti pulsators that resemble the W UMa binaries when the period is doubled.

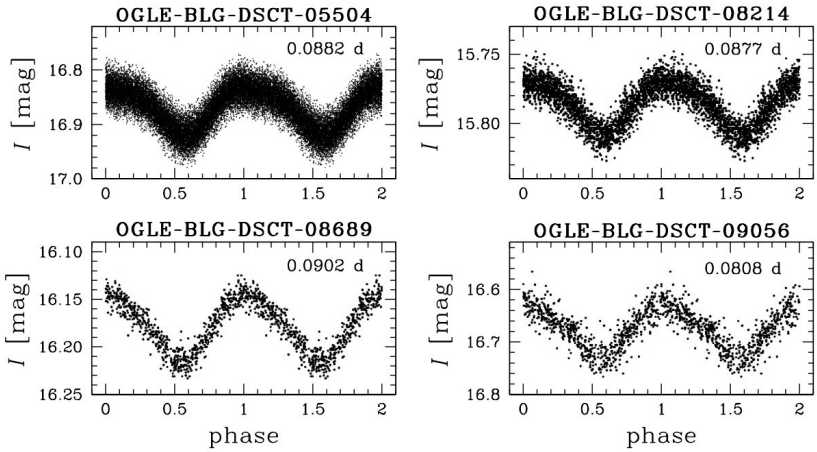

Figure 1.4: Example light curves of δ Scuti variable stars (Pietrukowicz et al. 2020).

Chapter 2

Characteritics of TIC 229741985

The first attempt at classifying the object studied in this thesis was made during a large-scale classification of A-F stars in the northern *TESS* continuous viewing zone described in Skarka et al. (2022). Using only photometric data from *TESS* all-sky mission (see chapter 3) and corresponding Fourier transform, a clear classification of the variability of TIC 229741985 could not be performed. The object was marked as either a δ Scuti variable according to its most significant frequency in the frequency spectrum that lies in the δ Scuti regime (approximately 11.49 c/d) or a W UMa binary system according to the shape of its light curve (assuming that the real frequency is half the most significant one). Fig. 2.1 shows the classification image from Skarka et al. (2022).

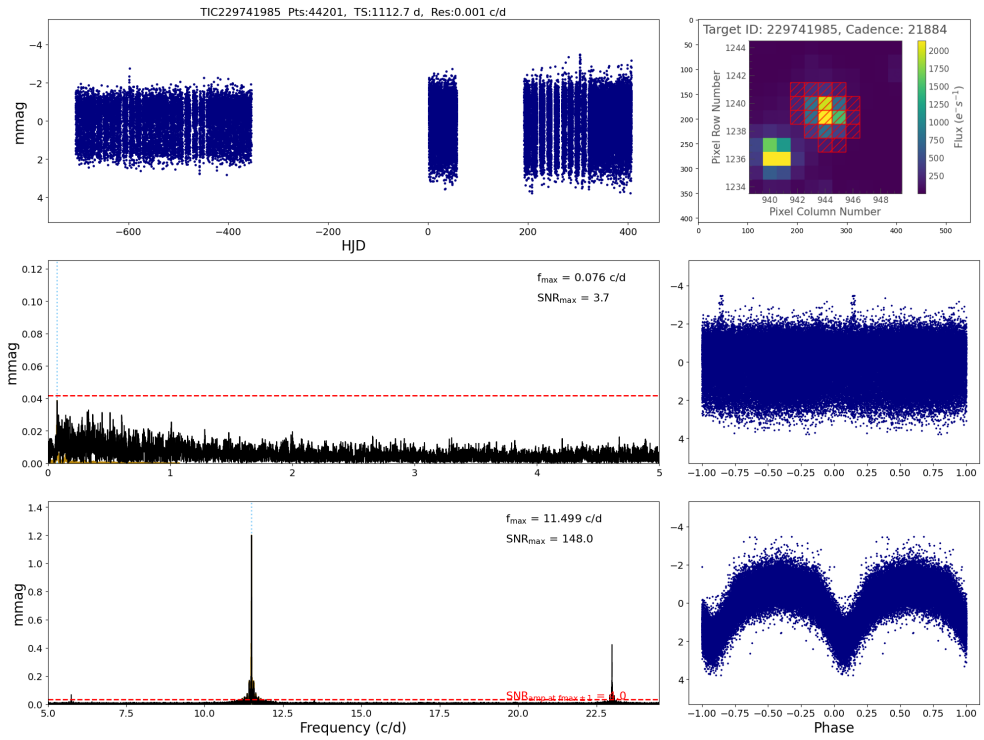

Figure 2.1: Classification image of the studied object from Skarka et al. (2022).

TIC 229741985 was assigned different designations used by various catalogs with astronomical data, some shown in Table 2.1. All known identifiers are provided by the SIMBAD database [E3]. The studied object is located in the Draco constellation. Its position in the equatorial coordinate

system is in Table 2.1, and its position in the selected sky region with a diameter of 20' is displayed in Fig. 2.2. The star is circumpolar for most of the northern hemisphere from the latitude of 19 degrees.

Table 2.1: Parameters of TIC 229741985

Parameters	**Values**	**References**
Identifiers	TYC 4438-48-1	[E3], accessed Feb 11, 2023
	GSC 04438-00048	[E3], accessed Feb 11, 2023
	Gaia DR3 2265748153772929408	[E3], accessed Feb 11, 2023
RA J2000 [°]	279.7694042015368	Gaia Collaboration et al. (2022)
DEC J2000 [°]	+71.3410112355028	Gaia Collaboration et al. (2022)
π [mas]	3.278 ± 0.012	Gaia Collaboration et al. (2022)
d [pc]	305.1 ± 1.1	calculated from π
	305.096	Gaia Collaboration et al. (2022)
	306.791	Paegert et al. (2022)
G [mag]	10.484	Gaia Collaboration et al. (2022)
$BP - RP$ [mag]	0.548	Gaia Collaboration et al. (2022)
Spectral Type	F5	[E5], accessed Feb 11, 2023
T_{eff} [K]	6722.959	Gaia Collaboration et al. (2022)
	6805.0 ± 126.1	Paegert et al. (2022)
$\log g$ [cms^{-2}]	4.1371	Gaia Collaboration et al. (2022)
	4.22 ± 0.09	Paegert et al. (2022)
M_{T} [M$_{\odot}$]	1.5 ± 0.3	Paegert et al. (2022)
R_{T} [R$_{\odot}$]	1.56 ± 0.06	Paegert et al. (2022)
L_{T} [L$_{\odot}$]	4.7 ± 0.2	Paegert et al. (2022)
A [mag]	0.054	Gaia Collaboration et al. (2022)

Gaia ESA Archive provides the value of absolute stellar parallax π at the reference epoch of the source [E1] and its standard error, used to establish the object's distance from the Earth. The relation between the distance in parsecs and parallax in arcseconds used for the calculation of the star's distance in Table 2.1 is

$$d = \frac{1}{\pi}. \tag{2.1}$$

The distance was also determined by the Gaia Archive (Gaia Collaboration et al. 2016) and from the data in the TESS Input Catalog (TIC)[1] (Paegert et al. 2022). For the data acquired from the Gaia mission, the distance calculated from the parallax corresponds to the determined value within the error bars.

Other parameters in Table 2.1 were taken from the Gaia mission and TESS Input Catalog accessed through Vizier. Monochromatic extinction A was determined from the spectral analysis of TIC 229741985 (Paegert et al. 2022).

[1] TIC catalog is further discussed in chapter 3.

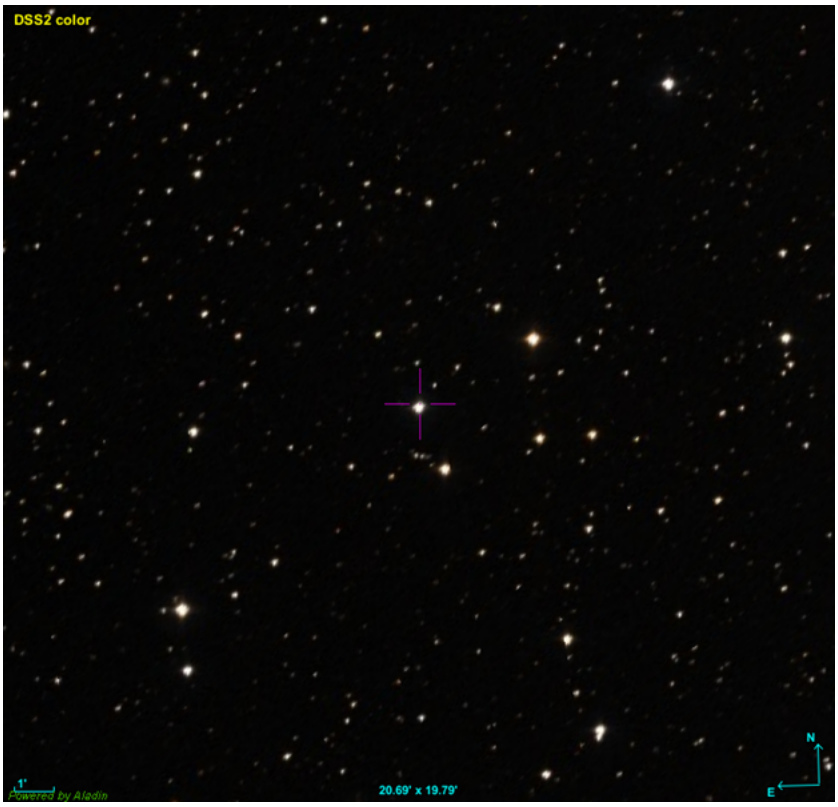

Figure 2.2: Sky region around TIC 229741985, image provided by the interactive Aladin sky atlas (Bonnarel et al. 2000) from the SDSS sky survey (Almeida et al. 2023).

Surface temperatures of the stars are defining parameters in stellar classification into spectral types. This classification system is based on the observed absorption lines in the spectrum of the studied object. The spectral type of TIC 229741985 was determined from the table on [E5] as F5.

Using data from the TESS Input Catalog Paegert et al. (2022), I determined the position of TIC 229741985 in the Hertzsprung–Russell diagram. Fig. 2.3 shows the location of various pulsating stars on the HR diagram taken from Skarka et al. (2022). The red circle added to the image represents an approximate location of TIC 229741985 in relation to the depicted instability strip.

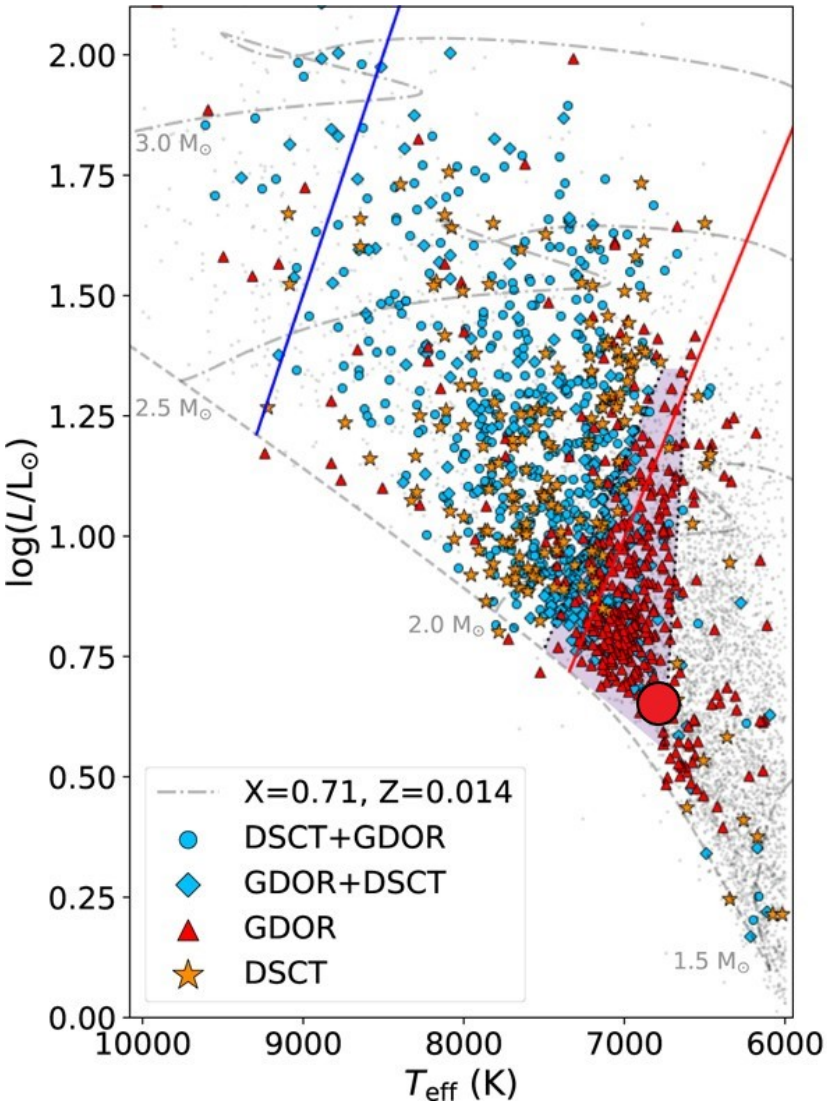

Figure 2.3: Location of pulsating variable stars in Hertzsprung–Russell diagram taken from Skarka et al. (2022). The dashed line represents the zero-age main sequence, and the continuous blue and red lines mark the edges of the instability strip taken from Murphy et al. (2020). The red circle represents an approximate location of TIC 229741985.

Chapter 3

Data Sources

3.1 Photometry

The main source of the photometric data used to analyze the light curve of TIC 229741985 and determine the origin of the observed variability was the *Transiting Exoplanet Survey Satellite (TESS)* (Ricker et al. 2015). Additional photometric measurements were obtained from my observations in the Kraví Hora and Vyškov observatory in the Czech Republic, using 60 cm and 50 cm reflecting telescopes, respectively.

TESS All-Sky Survey Mission

TESS is a space telescope designed to detect exoplanets orbiting around bright stars using the transit photometry method (Ricker et al. 2015). It is a followup to a *Kepler* mission (Borucki et al. 2010) that was launched nine years earlier to primarily observe Earth-size and smaller exoplanets near the habitable zone. Compared to *Kepler*, *TESS* studies stars 30 to 100 times brighter to allow subsequent observations with ground-based telescopes and radial-velocity measurements. The observed range of magnitudes for exoplanet host stars compared to the targets of *Kepler* mission is shown in Fig. 3.1.

TESS has an eccentric, high orbit around the Earth with 2:1 resonance with the Moon and an orbital period of 13.7 days, suggested by Gangestad et al. (2013) and shown in Fig. 3.2. Resonance of *TESS* and Moon periods provides further spacecraft stability without requiring extensive course-keeping corrections (Keesey 2017). The orbit's inclination eliminates Earth's and Moon's eclipses, which could interfere with the observations.

The instrument is comprised of four identical wide-field cameras, which cover a 24° by 96° region of the sky oriented along the ecliptic longitude, with one of the cameras centered on an ecliptic pole. Each camera's detector assembly comprises four identical CCD devices aligned into two by two matrix with gaps between individual CCDs less than 10' (Vanderspek et al. 2018). Each pixel represents an area of 20x20 arcseconds in the sky with stars typically spread in a 1-2 pixel radius (Stassun et al. 2018). The spacecraft does not pass through the Earth's radiation belt, providing a thermally stable environment for cameras, with temperature variations less than 0.01°C/h for most of the orbit. The lenses are optimized for a bandpass shifted into the red spectral region between wavelengths of 600-1000 nm. Earth-like exoplanets are being searched for around stars with spectral types G and K, whose emission of stellar radiation has maxima in this range (Vanderspek et al. 2018). Habitable zones around these stars are at such a distance that their stellar activity is not a problem for the potential life inhabiting the exoplanet.

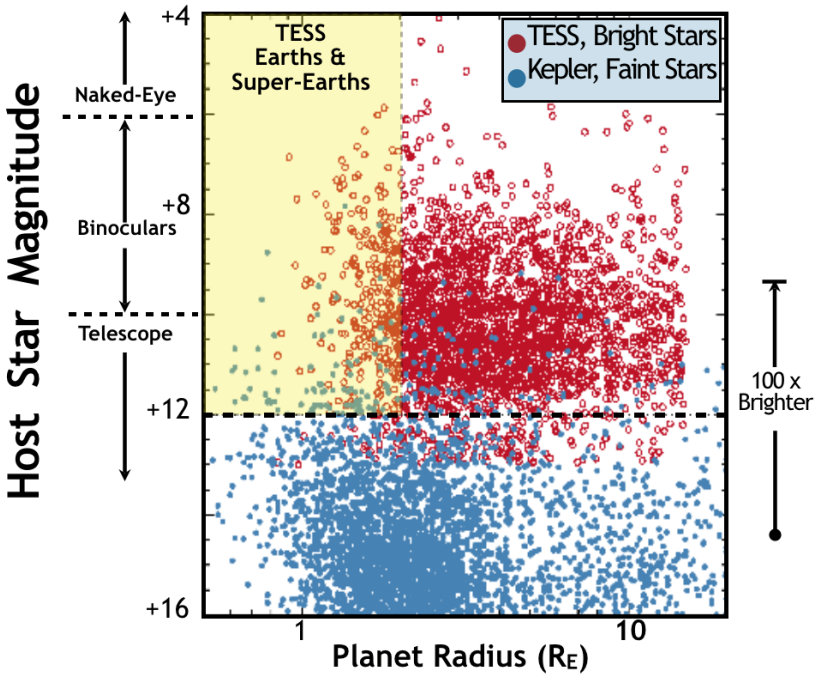

Figure 3.1: Potentional host stars observed by the *TESS* compared to the targets of *Kepler* mission (Barclay 2023*b*).

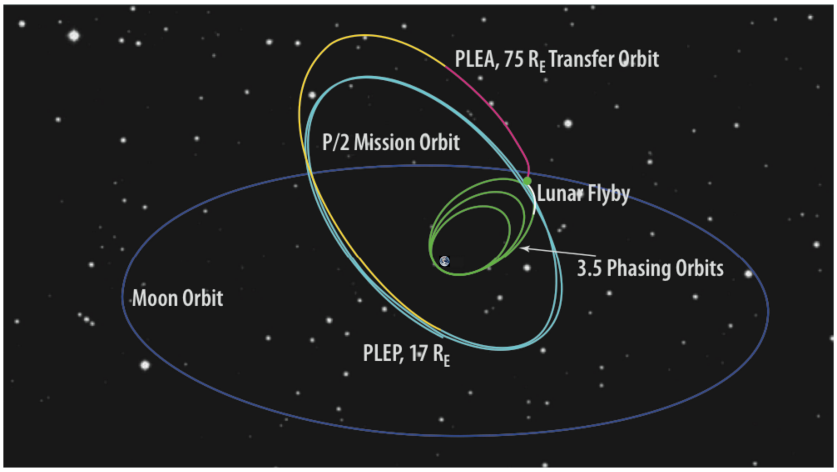

Figure 3.2: Schematic of maneuvers leading to the final *TESS* orbit marked by the light blue line (Ricker et al. 2015).

The scattering of light from bright objects in the sky increases the background sky level. *TESS* cameras are equipped with lens hoods to reduce the excess light reflected off Earth and the Moon. When one of these objects enters the camera's field of view, the increase in background levels and saturation of pixels make the observations useless.

The sky covered by *TESS* is divided into sectors, each observed for two spacecraft orbits (Barclay 2023*b*, 27.4 days). These sectors systematically cover the sky region between the ecliptic poles and the latitude of 6 degrees from the ecliptic, with increasing overlap toward the poles. Afterwards, the field of view (FOV) is shifted by approximately 26°, and the process repeats

(Vanderspek et al. 2018). The location of sectors observed during the mission is shown in Fig. 3.3. An offset from the ecliptic in some sectors was increased to 37 degrees to prevent interference of the light scattered from the Earth and Moon. The FOV of the extended missions is shifted and rotated to observe regions of the sky in the gaps between CCDs not covered during the previous missions (Barclay 2023*c*).

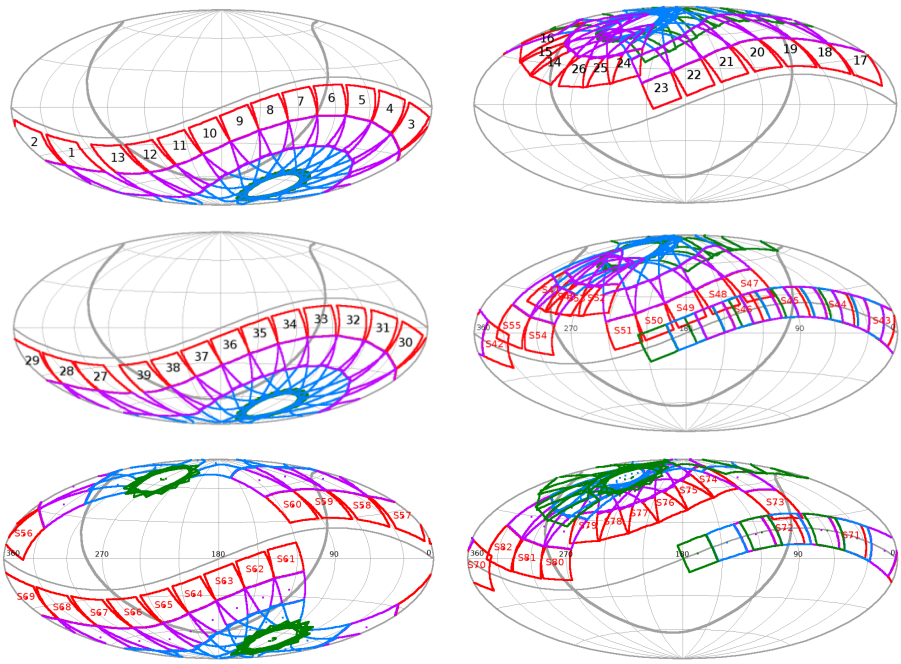

Figure 3.3: Sky coverage maps in the ecliptic coordinate system depicting the observed sky regions. The first row of schematics maps sectors covered during the primary mission, the second row depicts sectors observed during the first extended mission, and the third row shows sectors covered during the second extension of the mission (MIT n.d.).

Raw data from the spacecraft are processed by The Science Processing Operations Center (SPOC) at NASA Ames Research Center into calibrated pixels and lightcurves. *TESS* transmits the data at the orbit's perigee located 17 $R_{\odot}$ from Earth through the Deep Space Network. SPOC calibrates them by orbit and individual sectors using calibration models provided by the Massachusetts Institute of Technology Payload Operations Center (Jenkins 2015) and generates target pixel files (see below) and light curves of selected objects.

TESS cameras combine images with a 2-second exposure into a single image. There are three primary data products derived from the two-second observations (Twicken et al. 2020):

- **Full Frame Image (FFI)** - set of all pixels across all CCDs of a given camera. It was taken every 30 minutes during the primary mission, every 10 minutes during the first extended mission, and every 200 seconds during the second extension of the mission (see Fig. 3.3). FFIs are created onboard the spacecraft by co-adding the two-second observations in groups according to the desired exposure time. FFIs are provided as uncalibrated or calibrated files in FITS format.

- **Target Pixel File (TPF)** - set of pixels around a selected target with a 2-minute cadence with the addition of a 20-second cadence data from the first extension onward. They contain raw

data from pixels around a selected object with an aperture pipeline mask to indicate which pixels were selected and further processed.

- **Light Curve File (LCF)** - file containing time-flux dependency processed by SPOC pipeline from TPFs and FFIs and by the MIT Quick-Look Pipeline (QLP) from FFIs of selected targets.

Light curves processed by the SPOC pipeline from TPFs onboard the spacecraft have author names (provenance names) 'SPOC.' Author name 'TESS-SPOC' (Caldwell et al. 2020) refers to TPFs, and light curves derived directly from the FFIs by the SPOC pipeline with 30 min, 10 min, and 200s cadence. Light curves referred to as 'QLP' are produced by the MIT Quick-Look Pipeline from a set of stars with limited magnitude from the *TESS* Full Frame Images, further described in Huang et al. (2020*a*), Huang et al. (2020*b*), Kunimoto et al. (2021), Kunimoto et al. (2022).

The secondary data products include collateral data describing the calibration of pixels and auxiliary data products providing files with engineering and telemetry data for image calibration and documenting the spacecraft's state.

TESS uses the TESS Input Catalog (TIC) for target selection and creation of TPF and LCF files. The TIC contains over 473 million stars and provides astronomical information about possible targets for exoplanet detection, such as coordinates in an equatorial coordinate system, proper motions, magnitudes, and many more. A Candidate Target List (CTL) is a list of objects derived from the TIC that meet certain criteria for creating a list of high-priority targets optimized for detecting small planets (Stassun et al. 2018).

Data from the *TESS* mission are available for download in the Mikulski Archive for Space Telescopes (MAST) [E6] directly from the MAST Portal or through data analysis tools. In this thesis, I used LIGHTKURVE (Lightkurve Collaboration et al. 2018), a Python package for analyzing data products of *Kepler* and *TESS* space telescopes and time series data of variable objects. Through this package, I obtained light curve files from the SPOC, TESS-SPOC, and QLP pipelines with individual time-series data from different authors. I processed 17 SPOC light curves with an exposure time of 120 seconds, 13 TESS-SPOC light curves with an exposure of 1800 seconds, and 13 QLP light curves with 1800 seconds of exposure.

The raw data contain flaws from light scattering and detection of high-energy particles, manifesting as peaks in the light curves and deformed profiles due to long-term trends. Individual sectors have different mean magnitudes due to the conditions during observation, such as the background sky levels, relative position of other objects in the sky, and position of *TESS* in its orbit. The LCF files contain two types of measured flux: SAP Flux, calculated as a sum of the brightness in a chosen aperture mask, and PDCSAP Flux, with removed systematic trends (Barclay 2023*a*). A comparison of raw PDCSAP and SAP fluxes from the SPOC sector 57 is shown in Fig 3.4. An illustration of the raw PDCSAP data from all sectors in the TESS-SPOC pipeline is shown in Fig. 3.5.

LIGHTKURVE package allows for the automatic removal of outliers, the remnants of high-energy particle detection, and the removal of long-term trends by flattening the light curve. I used the `remove_outliers()` routine to eliminate the stray points in the graphs by sigma-clipping. Points deviating by more than 3σ were removed. Afterward, I used the `flatten()` function to remove long-term trends and artifacts from the detector. The individual sectors were then stitched together, as is shown in an example of the corrected light curve from the TESS-SPOC routine in Fig. 3.6. Comparison of corrected light curves in Fig. 3.7 clearly shows the light variations within a range of one day.

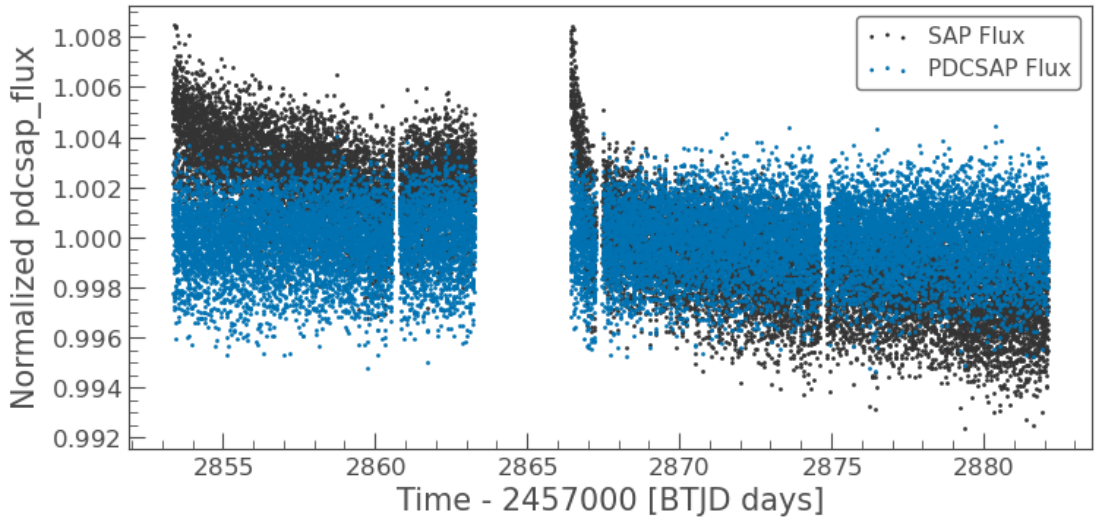

Figure 3.4: Comparison of raw PDCSAP and SAP flux produced by the SPOC pipeline.

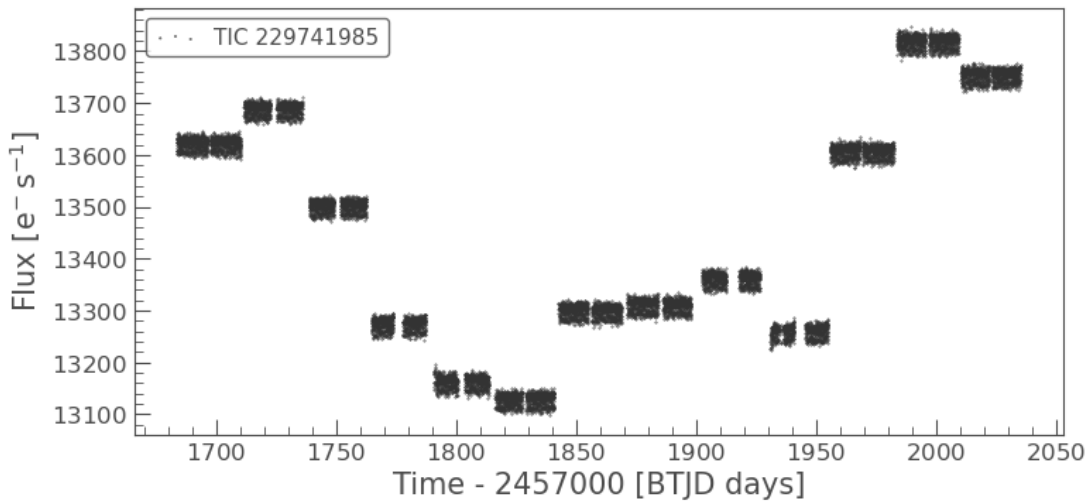

Figure 3.5: The raw PDCSAP photometric data produced by the TESS-SPOC pipeline.

Kraví Hora and Vyškov Observatory

Complementary material to *TESS* observations, original photometric observations, were gathered on Kraví Hora and Vyškov observatories. These additional measurements aimed to create light curves in different photometric filters and compare the amplitude of variations in the spectra's blue and red regions, which can help us better estimate the nature of the variations.

Observatory on Kraví Hora is located near the center of Brno and is maintained and operated by the Brno Observatory and Planetarium. The telescope has a primary mirror with a diameter of 60 centimeters and is equipped with a G2-4000 CCD camera observing with the Johnson-Cousins UBVRI photometric filters [E7]. The observatory was founded in 1948 with the help of the Astronomical Institute of Masaryk University members and was maintained by the Department of theoretical physics and astrophysics until 2020 [E8]. The observing site's quality deteriorated with Brno's expansion around the observatory. The low elevation of approximately 310 meters above

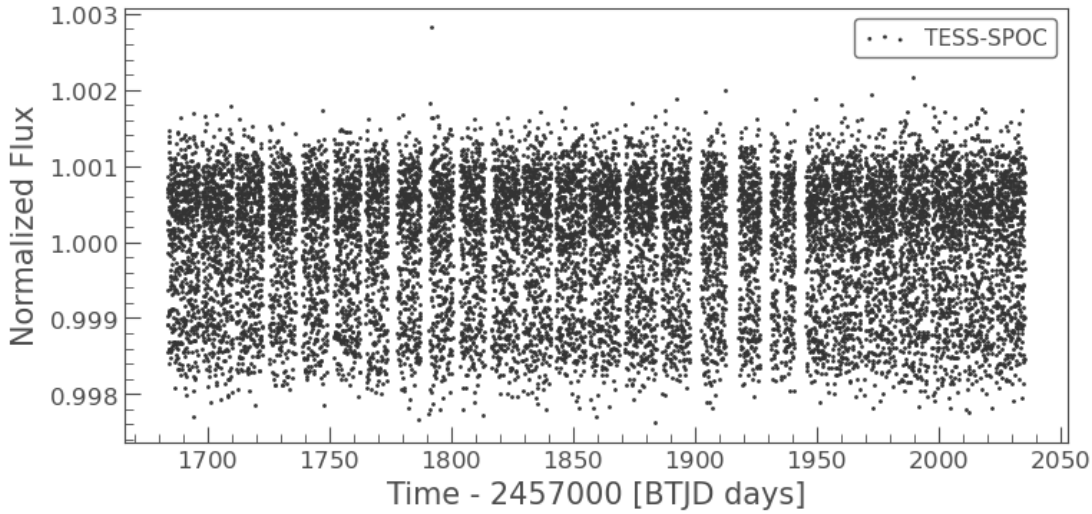

Figure 3.6: The corrected and used photometric data of TESS-SPOC.

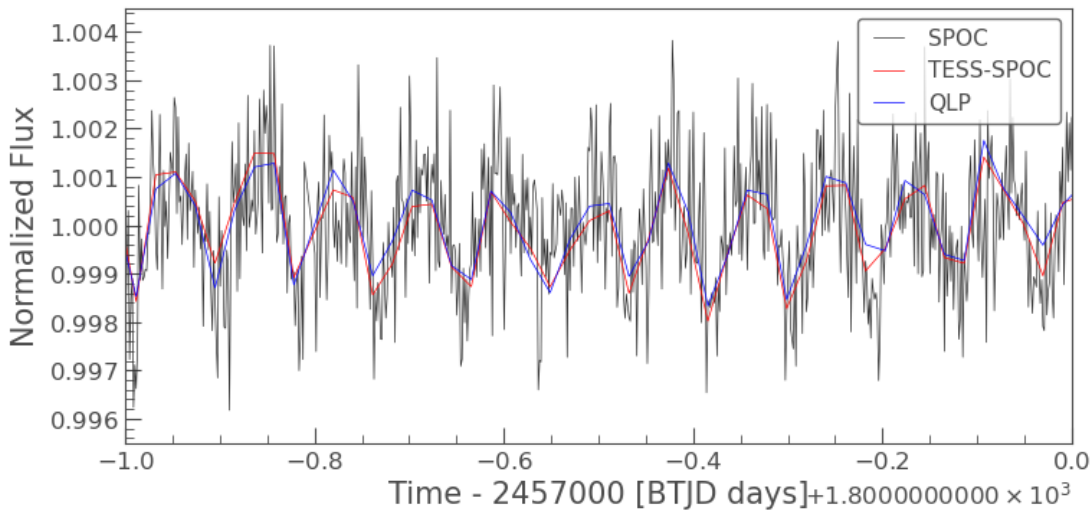

Figure 3.7: The corrected light curves of SPOC, TESS-SPOC, and QLP routines measured during one day.

sea level, pollution from traffic, industry, and light pollution limit the observations to a few dozen days a year with the restricted observing season (Mikulášek et al. 2000).

Compared to the Kraví Hora observatory, observational conditions in Vyškov observatory are much better thanks to its distance from towns and other sources of light pollution. The observatory is maintained and operated by ZOO PARK Vyškov. Newtonian reflecting telescope with a diameter of 50 cm that was mounted in 2014 and uses a CCD camera with Johnson-Cousins UBVRI photometric filters [E9].

TIC 229741985 observations on Kraví Hora observatory yielded 94 images taken in the B photometric filter with 60-second exposure times and 94 images in the I photometric filter with 40-second exposition. Before extracting a light curve, the acquired images must be corrected. Pre-processing of the images eliminates the influence of a telescope and the effects caused by a CCD camera, such as a dark current, zero offsets, vignetting, etc. Dark current refers to a small electrical

current generated by charged particles from the detector when no light enters the camera and is proportional to the temperature of the CCD and exposition time. From the images, I subtracted a master dark frame. This image maps the dark current inside the used camera calculated as the median of several dark frames with the exposition time identical to the corrected frames. Another important correction is the division of the images by a master flat-field from the same photometric filter. Flat-field frame smoothens any light variations caused by the different sensitivity of the individual pixels, dust shadows on the telescope's filters, filter non-homogeneity, and vignetting. Unfortunately, I could not obtain them on the same night as the rest of the images. The additionally measured flat-fields worsened the quality of observations, so I omitted this part of the correction. The images in the respective photometric filters and dark frames were made on October 7 from 5:33 PM to 1:15 AM, with flat fields measured on October 19 from 4:00 PM to 4:13 PM. All observations were processed using MUNIPACK (Hroch 2014).

In Vyškov, I was able to gather 124 images in the photometric filter *B* and 124 images in the photometric filter *I*, both with the exposition of 60 seconds. The scientific and dark-frame exposures were made on October 9 from 5:48 PM to 1:26 AM. The images were corrected with a master dark frame and constructed by median-averaging individual dark frames. Flat fields could not be obtained because of the observing conditions during the night. The pre-processed images in *I* filter from both observing sites are compared in Fig. 3.8.

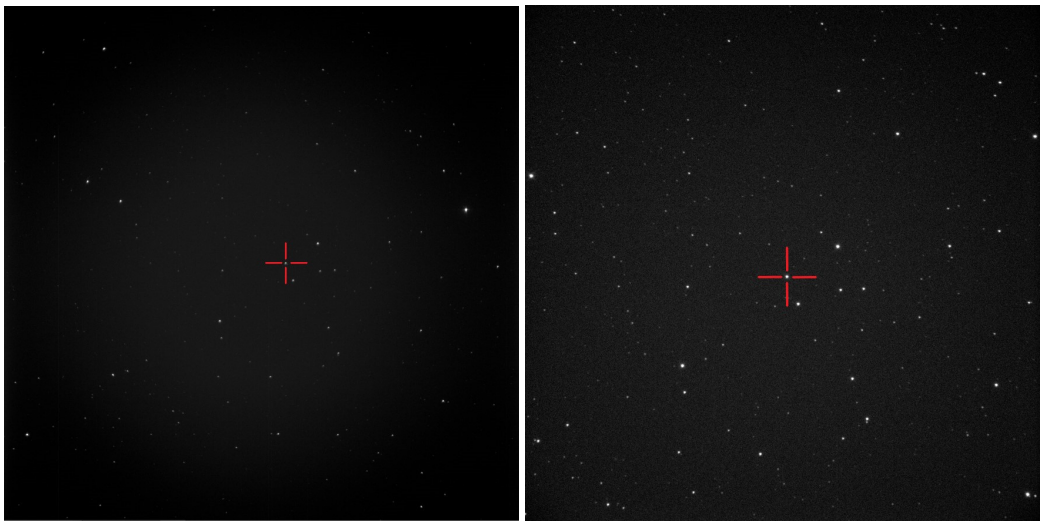

Figure 3.8: Calibrated images of TIC 229741985 in photometric filter *I* from Kraví Hora observatory (image on the right) and from the Vyškov observatory (image on the left). In both images, TIC 229741985 is marked with a red cross.

When the calibrated images were prepared, I used MUNIPACK routines to detect stars on all frames and do astrometry and differential photometry calibration, which extracted the magnitudes in the relevant filter by comparing the flux from TIC 229741985 to the flux of non-variable stars in its vicinity. The automatic routine in MUNIPACK identified reference stars from the UCAC4 catalog. I constructed light curves for both filters shown in Fig. 3.9. Due to the less-than-satisfactory conditions during the observation nights, such as the light pollution and low clouds, many images were useless, manifesting as gaps in the extracted light curves.

Due to the poor observing conditions and relatively faint target with amplitude variations around 1-2 mmag in the TESS passband, the variability of TIC 229741985 cannot be deduced from the observations gathered in Brno and Vyskov. These data are not further used in the thesis.

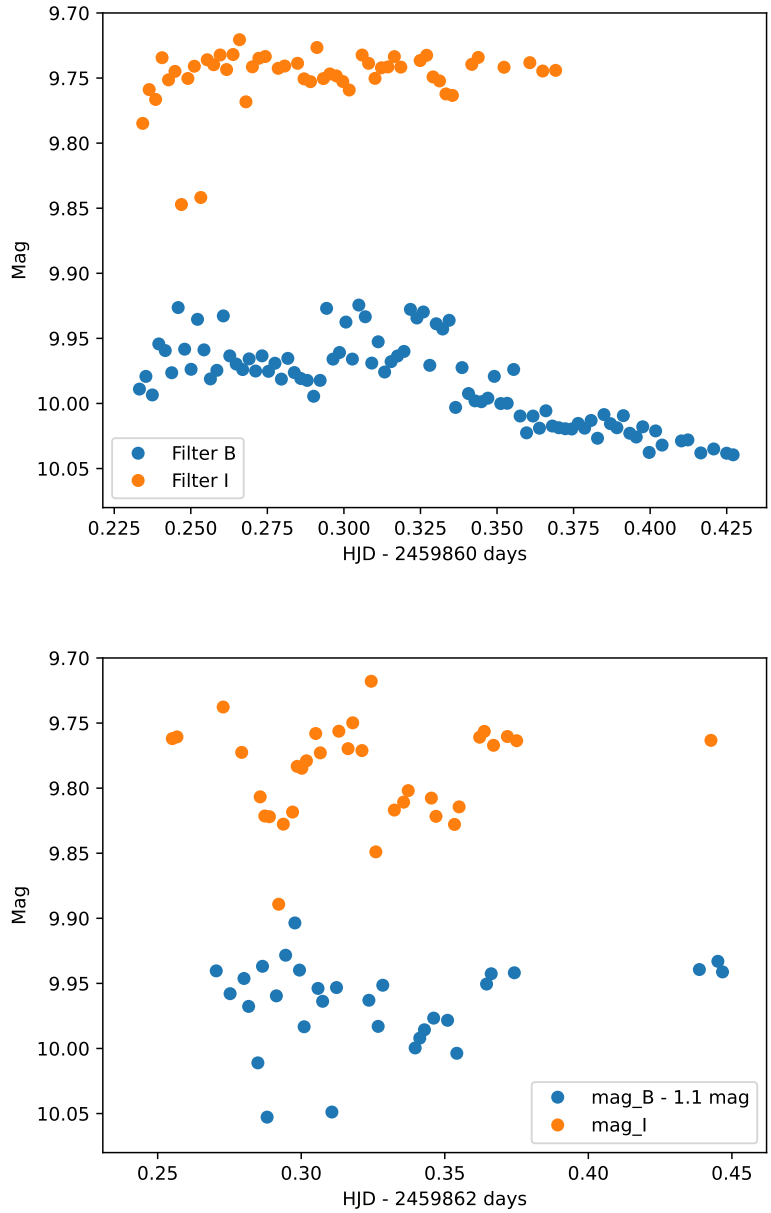

Figure 3.9: Light curves of TIC 229741985 observed in photometric filter *B* and *I* on Kraví Hora observatory (top image) and on the Vyškov observatory (bottom image).

3.2 Spectroscopy

Spectroscopic observations by ground-based telescopes are essential for further analysis of objects measured in photometric sky surveys like *Kepler* or *TESS*. Follow-up observations differentiate between candidates for exoplanets and false positives, such as binary star systems or pulsators, and provide additional information about the studied objects. Spectral analysis of TIC 229741985 aimed to measure the radial velocities of the studied object and determine the presence of a companion from the shift in spectral lines.

All spectroscopic observations of TIC 229741985 used in this thesis were obtained with Ondřejov Echelle Spectrograph (OES, Koubský et al. 2004, Kabáth et al. 2020). connected to the Perek telescope located in Ondřejov, approximately 30 kilometers from Prague. The primary mirror has a diameter of 2 meters. Echelle spectrograph uses a diffraction grating with a particular shape of its elements to display high diffraction orders, which increase the spacing of spectral features (Chaffee & Schroeder 1976). An example of a two-dimensional spectrum obtained with OES is shown in Fig. 3.10. The individual spectral orders are imaged as nearly horizontal parallel lines at a CCD chip, which makes the data reduction of these spectra complex and very sensitive to the reduction process (Škoda et al. 2008). OES was built in 2007 at the Stellar department of the Astronomical Institute of the Academy of Sciences of the Czech Republic and installed in a thermally stable room beneath the Perek telescope at its coudè focus.

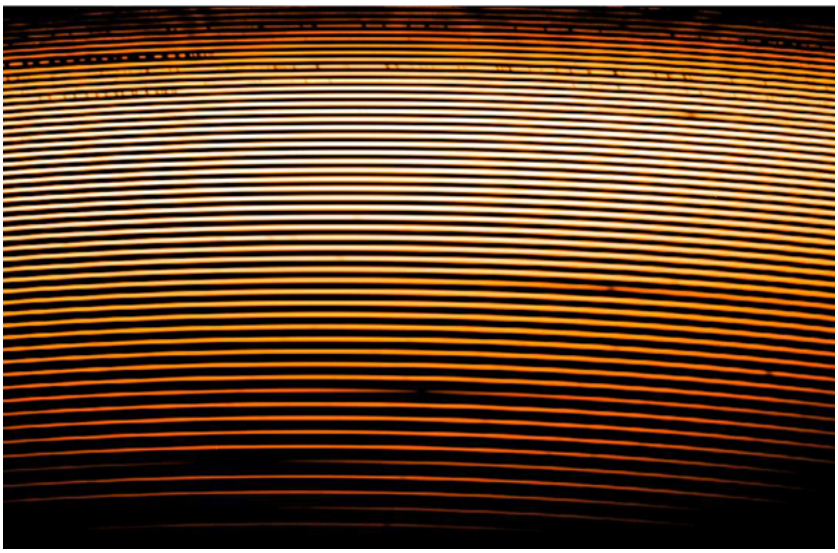

Figure 3.10: Part of echelle spectra of Vega from Ondřejov Echelle Spectrograph (Škoda et al. 2008).

The observing site is located in an area with minimal light pollution and typical seeing between $2-3''$, which allows the observation of objects to the 13th magnitude in the V filter. Due to the location's climate and weather conditions, only 25-30% of the observing hours throughout the year yield good data (Kabáth et al. 2020).

From August to November 2022, eleven spectra of TIC 229741985 were gathered from the Ondřejov Echelle Spectrograph . Table 3.1 shows the expositions, times of the observations, and respective Julian dates of the beginning of the expositions for individual spectra. The exposure time was chosen in such a way as to obtain a sufficient signal-to-noise ratio (SNR) and, at the same time to have a good cadence due to the short period. The spectra were processed in IRAF - a software package for spectral data reduction (Tody 1986). SNR of the individual spectra was computed by `splot` routine in IRAF as mean divided by the root mean square within a specific range. I used a range with a small number of spectral lines between 6600 and 6860 Å.

The raw spectra produced by the echelle spectrograph have many defects caused by the instruments used for their observations and unwanted detections of high-energy particles. A bias frame was used to correct the raw images and remove the noise of the CCD camera, with subsequent removal of bad pixels and pixels affected by the impact of high-energy cosmic radiation. Afterwards, individual apertures had to be identified and extracted. One of the problems in reducing echelle spectra is the removal of the grating blaze function, which reduces the intensity of the spectrum

Table 3.1: Information about individual spectra obtained by the OES.

	Date [yyyy-mm-dd]	Time [hh-mm-ss]	JD	Exptime [s]	SNR
1	2022-08-29	19-20-01	2459821.30557	3600	24.5
2	2022-10-09	17-57-04	2459862.24796	2400	22.3
3	2022-10-09	18-43-49	2459862.28043	2400	22.3
4	2022-10-09	19-24-32	2459862.30870	2400	19.7
5	2022-10-09	20-05-15	2459862.33698	2400	15.5
6	2022-10-09	20-45-58	2459862.36525	2400	12.5
7	2022-10-09	21-26-41	2459862.39353	2400	15.0
8	2022-10-09	22-07-24	2459862.42181	2400	13.8
9	2022-10-09	22-48-07	2459862.45008	2400	14.5
10	2022-10-09	23-28-50	2459862.47836	2400	13.5
11	2022-11-02	16-57-31	2459886.20661	2400	19.9

toward the edge of each order and strongly influences the shape of the object's continuum (Škoda et al. 2008). By defining the regions between individual spectral lines, the continuum was fitted with a polynomial and flattened to reduce the blaze function's influence. After identifying spectral lines, wavelength calibration, and stitching the apertures together, I obtained a 1D spectrum of TIC 229741985 from the individual exposures.

Fig. 3.11 is a cutout from the TIC 229741985 spectra around the Mg I triplet and a spectral line Hα indicating the quality of the given observation. The spectrum from August had the best SNR and was used as a template for the relative velocity calculations.

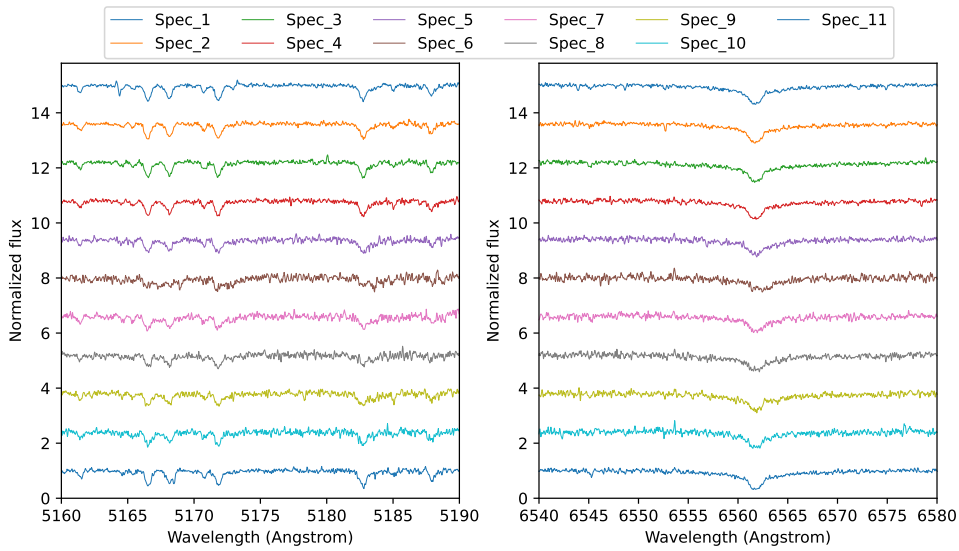

Figure 3.11: A cutout of TIC 229741985 spectra showing the Mg I triplet and Hα spectral line and the noise of spectra continuum.

Chapter 4

Data Analysis

4.1 Origin of the Variable Signal

Because *TESS* has a very small angular resolution (21”/px), signals from nearby objects can mix in very easily. Therefore, verifying that the signal comes from a particular object, not from a nearby star, is necessary.

TIC 229741985 and the stars located within 2′ radius are shown in Fig. 4.1. The stars identified in Fig. 4.1 were numbered according to their brightness in the *G* band [E4], the brightest object in the set labeled as number one being TIC 229741985. Data for these objects, including their brightness, were gathered from the Gaia DR2 catalog and are listed in the appendix in Table A.1.

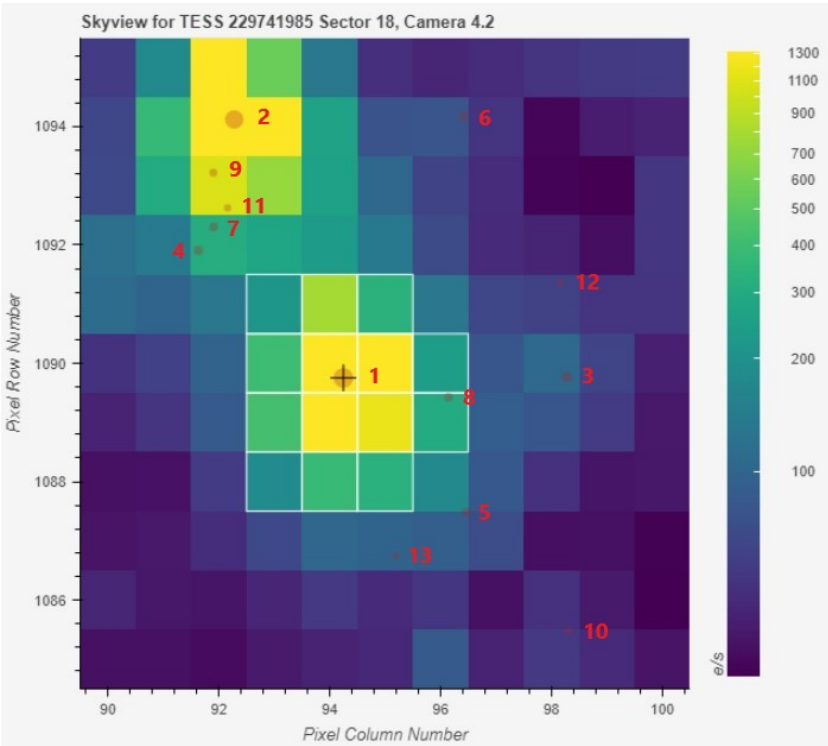

Figure 4.1: The TPF from sector 18 showing close vicinity of TIC 229741985.

For the analysis of photometric data of TIC 229741985, I used an aperture mask determined by the data processing pipeline (for sector 18 highlighted with white squares in Fig. 4.1). There

are two possible contaminating stars; a bright star with the number two (0.427 mags fainter than the target) and star number 8 (6-mag fainter than the target). If the signal came from the fainter star, amplitude variations would be visible only in the pixels containing the fainter source (the two most-right pixels). Contamination from the bright object would be, on the other hand, visible in the outer pixels of the selected aperture mask near the bright source with number 2.

Detailed examination of individual pixels can reveal the source of the observed variability. Using the LIGHTKURVE package, I constructed pixel maps (task `tpf.plot_pixels`) for all the sectors (Fig.A.1-A.15 in Appendix) detailing the frequency spectra on individual pixels in TPFs. The TPF of sector 18 is shown in Fig. 4.2 with the aperture highlighted by red squares. All pixels inside the aperture mask across all sectors contain the frequency peak at 11.49 c/d. In contrast, pixels around the bright star in the upper-left corner of Fig. 4.2 do not show the same frequency, eliminating the possibility of data contamination from star number 2 in Fig. 4.1. Furthermore, the faint source with the number 8 in Fig. 4.1 would not produce changes in the distant pixels. Therefore, the origin of light variations is TIC 229741985.

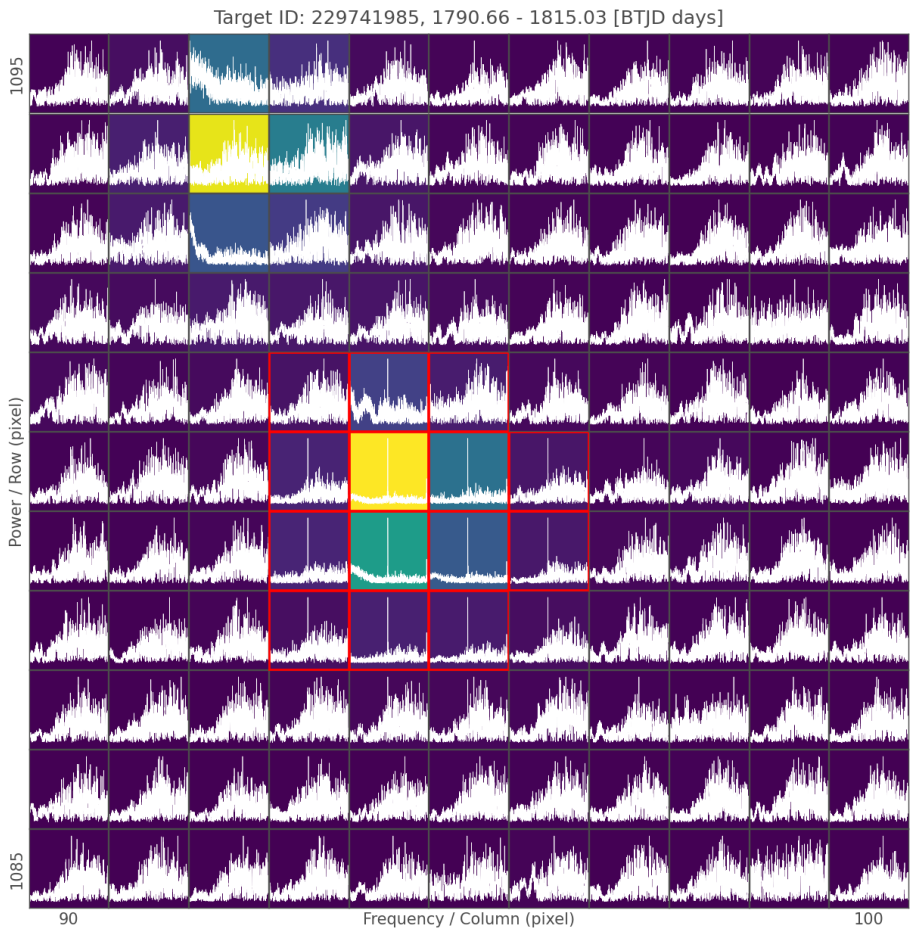

Figure 4.2: Pixel map of TIC 229741985 (sector 18) showing frequency spectra in different pixels with an aperture mask highlighted by red squares. The frequency range in each pixel is 0-23.5 c/d.

4.2 Time Series Analysis

The variability of stars is determined by periodic events that correspond with periods of light changes observed in the measured data. Light curve analysis is a basic procedure for understanding the time changes in the flux of variable objects. One of the basic goals of the time-series analysis is the determination of the measured signal's periodicity and the identification of fake periods, trends, and aliases. Fake periods are the results of periodicity in systematic errors during data reduction. They can be easily fixed by comparing the light curve of a variable object to a non-variable star subjected to the same data reduction process. Aliases arise as a result of the measurement's sampling rate and can be described using Tanner's relation (Mikulášek & Zejda 2013):

$$\frac{1}{P_{\mathrm{k}}} = \left| \frac{1}{P} + \frac{k}{P_{\mathrm{v}}} \right|; \; k = \pm 1, \pm 2, \ldots. \tag{4.1}$$

P_{k} is the period of an alias, P is the real period, and P_{v} is a sampling period, for example, for Earth-based observations, the sampling periods are typically one day, one year, etc.

Various methods for detecting and analyzing periodicity in discrete data sets, such as astronomical observations, have been developed to find repeating patterns in evenly or unevenly spaced values. In this work, I will use a discrete Fourier transform for period analysis of the extracted light curve. For a continuous signal $g(t)$, the Fourier transform $\hat{g}(f)$ is given by relation from VanderPlas (2018), where f is the frequency of the signal and $\mathrm{d}t$ is the infinitesimal time step:

$$\hat{g}(f) \equiv \int_{-\infty}^{\infty} g(t) e^{-2\pi i f t} \mathrm{d}t. \tag{4.2}$$

Information about the frequencies can be fully recovered only if the signal lies between the frequencies $\pm f_{\mathrm{c}}/2$, where f_{c} is the sampling rate of the data. This condition is known as the Nyquist limit. The Rayleigh frequency criterium determines the lowest resolvable frequency as f_{c}/N, where N is the number of data points.

The real observations have a finite number of samples, and the continuous function is subject to sampling at regular intervals Δt. We can substitute the Fourier integral for a Fourier sum with N evenly-spaced time steps:

$$\hat{g}(f) = \sum_{n=0}^{N} g_n e^{-2\pi i f n \Delta t}. \tag{4.3}$$

The power spectrum of a function represents a positive function with real values depending on the frequency and measures the degree to which each frequency f contributes to the overall signal. This function is computed as a squared amplitude of the Fourier transforms. Classical periodogram, also known as Schuster periodogram, is computed from the discrete Fourier transform using the relation:

$$P_{\mathrm{S}}(f) = \frac{1}{N} \left| \sum_{n=0}^{N} g_n e^{-2\pi i f n \Delta t} \right|^2. \tag{4.4}$$

To determine the period of light variations, I used PERIOD04 (Lenz & Breger 2005), software for analyzing time series data containing gaps. PERIOD04 uses a discrete Fourier transform algorithm to construct a frequency spectrum for unevenly spaced data sets. Fig. 4.3 shows the calculated frequency spectra for data produced by different pipelines.

In the computed spectra in all pipelines, I identified all significant peaks with SNR > 4 shown in Fig. 4.3. The frequency peaks are not independent and can be interpreted as f_0, $f_0/2$, and harmonics of f_0, as seen in Fig. 4.3. Frequency f_0 could be the harmonic of frequency $f_0/2$ if

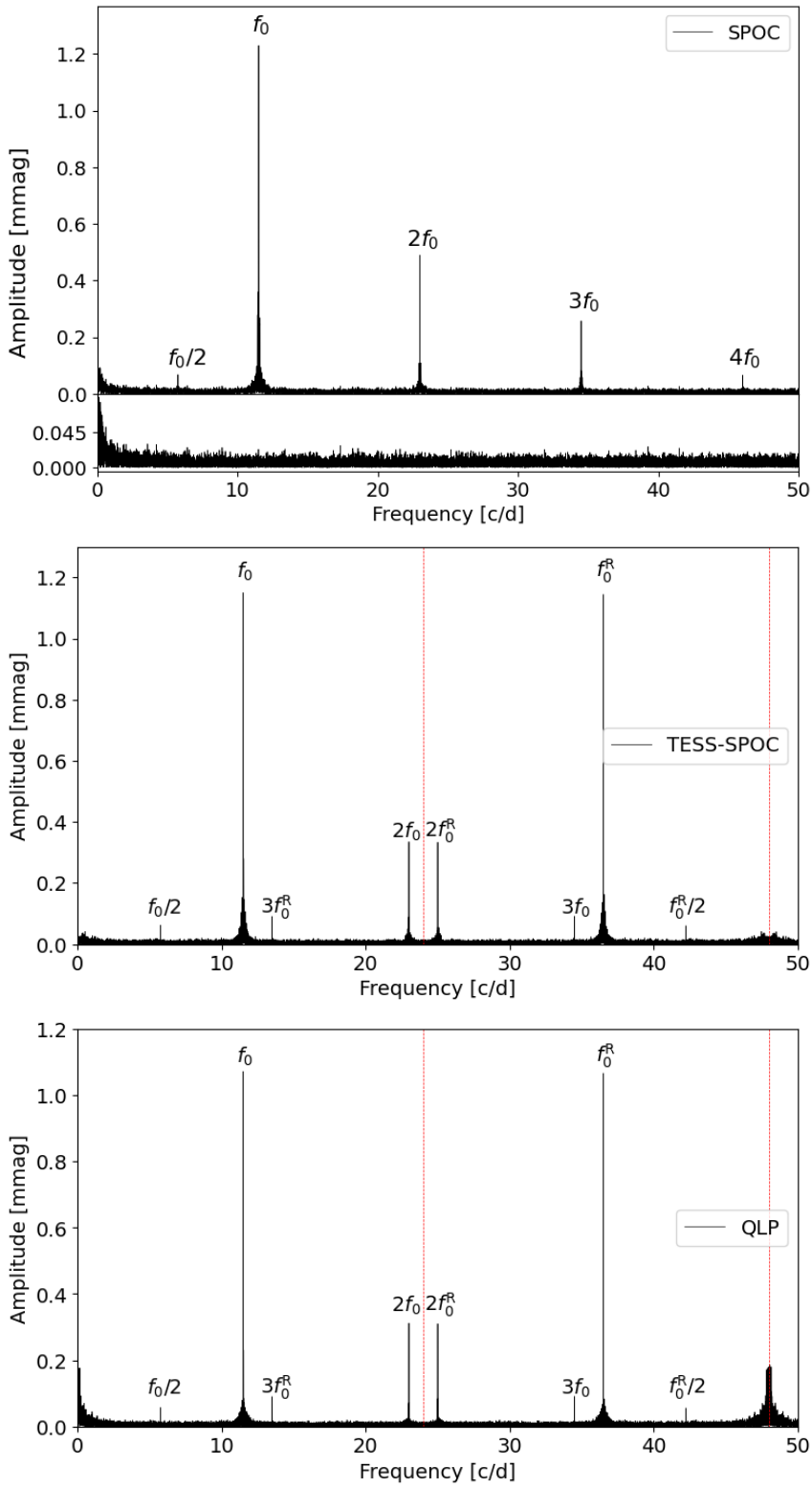

Figure 4.3: Fourier spectra of SPOC, TESS-SPOC, and QLP routines in a frequency range 0-50 c/d, with residua for the SPOC pipeline. The red vertical lines represent the Nyquist frequency and its harmonic at 48 c/d.

Table 4.1: Frequency values in SPOC, TESS-SPOC, and QLP pipelines.

		f [d^{-1}]	SNR	Δf [d^{-1}]	f_R [d^{-1}]
SPOC	f_0	11.498813(11)	40.1		0.00738
	$f_0/2$	5.7494851	7.9	0.000079	
	$2f_0$	22.9975054	33.1	0.000121	
	$3f_0$	34.4962581	24.3	0.000181	
	$4f_0$	22.9975054	8.5	0.000276	
TESS-SPOC	f_0	11.498815(5)	60.98698		0.00313
	$f_0/2$	5.7493142	10.1	0.000093	
	$2f_0$	22.9976834	40.9	0.000053	
	$3f_0$	34.4965962	14.1	0.000151	
QLP	f_0	11.49891(9)	75.7		0.00321
	$f_0/2$	5.7492572	9.0	0.000198	
	$2f_0$	22.9976031	43.4	0.000219	
	$3f_0$	34.4964056	14.7	0.000327	

we consider $f_0/2$ to be the real frequency. Table 4.1 shows the values of individual peaks in all pipelines with their respective SNR and errors calculated using LC FIT because PERIOD04 underestimates real error calculations for harmonics. The difference between the frequency peak's detected position and the respective harmonic's expected value is marked as Δf. The value of Δf is smaller than the calculated Rayleigh criterium f_R, which indicates that all identified frequencies are not independent.

The Nyquist frequency for the SPOC pipeline was 359.1 d^{-1} and 24.0 d^{-1} for the QLP and TESS-SPOC pipelines, respectively (marked in Fig. 4.3 with a dashed vertical line). Nyquist reflections of the real frequencies are labeled with 'R' in the superscript in Fig. 4.3.

The long-cadence data show additional frequency at $3f_0^{\mathrm{R}}$ =13.5036 c/d, which is not present in the SPOC pipeline, as shown in Fig. 4.3. This is a Nyquist reflection of $3f_0$. Instrumental effects cause frequency peaks close to 0 c/d in all pipelines and even multiples of Nyquist frequency.

Fig. 4.4 compares individual frequency spectra from different routines around the dominant peak. After subtracting the significant harmonics up to $4f_0$, I have not identified any other significant frequency (see the SPOC residuals in the top panel of Fig. 4.3). Frequency f_0 corresponds to the hypothesis that the studied object is a δ Scuti pulsator with f_0 being the main pulsation frequency. In contrast, the halved frequency $f_0/2$ can indicate that the system is a binary star, according to the shape of the phase diagram created using the period $P_{\mathrm{f}_0/2}$ (see below). The details are further discussed in the following sections.

Periods of pulsations are derived from the respective frequencies from the TESS-SPOC pipeline because the periodogram offered the most precise frequency calculations, thanks to the largest data set. The values are:

$$P_{\mathrm{f}_0} = 0.08696548\,(3)\,\mathrm{d},$$
$$P_{\mathrm{f}_0/2} = 0.17393096\,(16)\,\mathrm{d}.$$

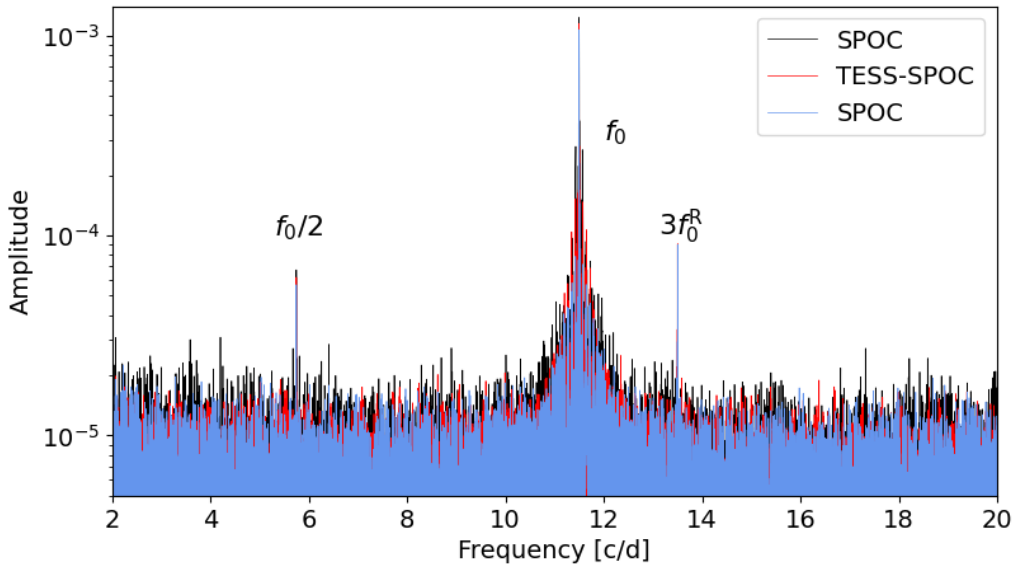

Figure 4.4: Comparison of Fourier spectra for different routines between frequency 0 and 20 c/d.

4.3 Pulsation Hypothesis

According to the amplitude and observed period of light variations, one of the possible explanations for TIC 229741985 light changes is the hypothesis that the studied object is a pulsating star of the δ Scuti type. In this section, I will present data corresponding to the pulsation hypothesis and utilize photometric observations and catalog data to verify the pulsational nature of the light variations. Phase diagrams have been constructed using period P_{f_0}. Fig. 4.5 shows the relation between phased data in the SPOC pipeline and binned curve, and Fig. 4.6 compares the binned phase diagrams of individual pipelines. Each dataset was divided into 51 equal-width bins, and the arithmetic mean of each bin was calculated. The shape of δ Scuti light curve may be reminiscent of W UMa binary system, as is shown on δ Scuti example light curves displayed in Fig. 1.4.

The phase diagram contains magnitudes on the vertical axis and a phase value on the horizontal axis. Using Pogson's equation, I obtained relative magnitudes from the relative flux around zero. By adding the magnitude from the TIC catalog, I received calibrated magnitudes for the studied object in the *TESS* photometric system. The phase of each point was determined using the following relation:

$$\theta = (t - t_0) \bmod P, \tag{4.5}$$

where t_0 is the moment of the first minima, P is the period of light variations, and t is the time of the procured data points. The time of the first minima was visually estimated as $t_0 = 24\,571\,790.74$ d, corresponding with the first minima observed in the SPOC data.

Using the information gathered from the Gaia Archive and TIC displayed in table 2.1, I calculated luminosity, radius, and mass and verified whether a system with such parameters could exist. I corrected the calibrated magnitude G from the Gaia Archive by extinction A, displayed in table 2.1 and applied bolometric correction $BC = 0.109$ mag determined by Jordi et al. (2010) to the absolute magnitude in G calculated from the Pogson's equation. Calculated parameters of TIC 229741985 with their respective errors corresponding to the pulsation hypothesis are listed in table 4.2 in the

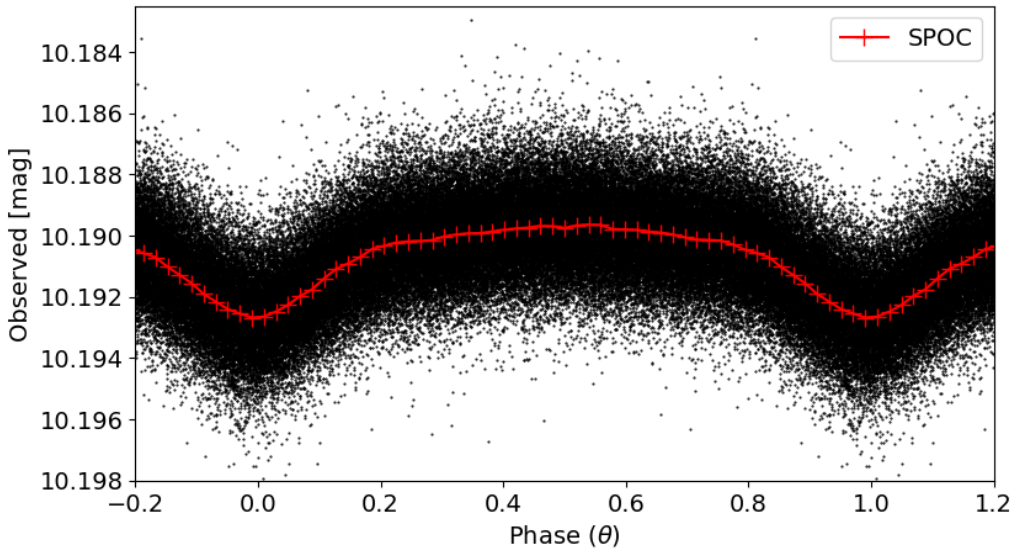

Figure 4.5: Phase diagram with binned data plotted over the light curve in SPOC corresponding to the pulsation hypothesis.

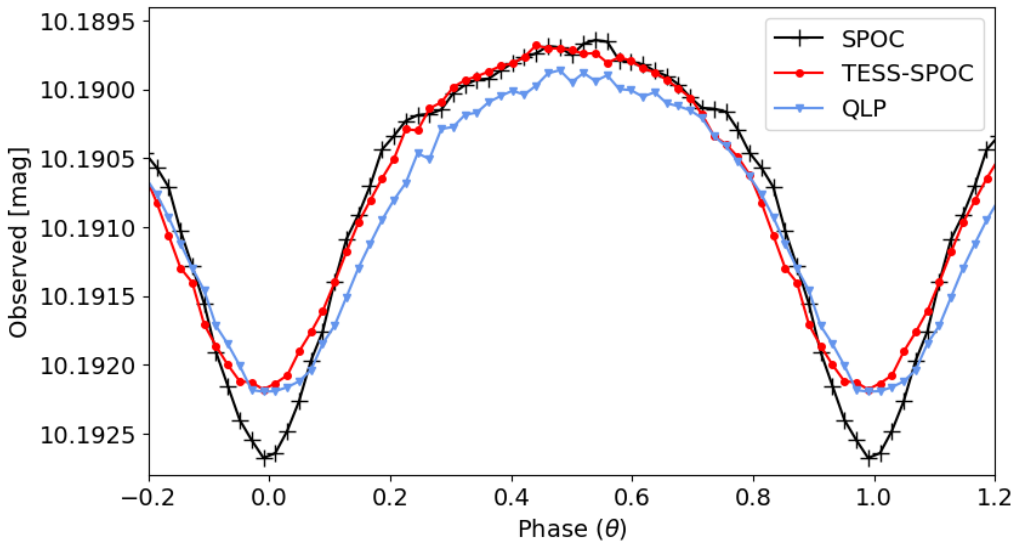

Figure 4.6: Comparison of phase diagrams with binned data for the SPOC, TESS-SPOC, and QLP pipelines.

'Single-star hypothesis' column. Effective temperature from the Gaia Archive, shown in table 2.1, was used to determine the star's radius R, which appears in the equation:

$$L = 4\pi R^2 \sigma {T_{\mathrm{eff}}}^4, \tag{4.6}$$

where L is the luminosity of TIC 229741985 estimated from the bolometric magnitudes ($M_{\mathrm{bol}} = 3.198(8)$ mag) and the distance d calculated from the parallax (see table 2.1). According to the shape of the TIC 229741985 light curve for binary star hypothesis (discussed in section 4.4), which has almost the same minima, I assume similar temperatures of stars, the same radii and masses of both components and, therefore, the same luminosity. The luminosity of individual components will be half the luminosity L calculated from the distance and bolometric magnitudes. The mass M was calculated from $\log g$ in table 2.1. I used equation 1.1 and period $P_{\mathrm{f_0/2}}$ to calculate the semi-major axis a, assuming that individual components in W UMa binary system have identical parameters as listed in column 'Binary star hypothesis' in Table 4.2.

Table 4.2: Parameters of TIC 229741985

Parameters	**Single-star hypothesis**	**Binary star hypothesis**
L [$\mathrm{L}_\odot$]	4.51 ± 0.03	2.25 ± 0.02
R [$\mathrm{R}_\odot$]	1.57 ± 0.06	1.11 ± 0.04
M [$\mathrm{M}_\odot$]	1.23 ± 0.09	0.61 ± 0.05
a [$\mathrm{R}_\odot$]		1.41 ± 0.04

The calculated values of luminosity and radius for a single-star hypothesis correspond with the values from the TIC shown in table 2.1. The calculated mass of TIC 229741985 was closer to the value of the sun's mass than the mass M_{T} from the TIC catalog in table 2.1, but its value was within M_{T} errors. Parameters for a binary star hypothesis are vastly different from the values in catalogs because, in them, TIC 229741985 was considered a single star.

Most δ Scuti variables are stars with pulsation periods shorter than 0.3 d and low amplitudes (< 0.1 mag). They lie in the lower part of the instability strip on the intersection with the main sequence in the mass range of 1.5 to 2.3 $\mathrm{M}_\odot$ for population I stars and 1.0 to 1.3 $\mathrm{M}_\odot$ for population II stars (Pietrukowicz et al. 2020). The theoretical boundaries of the instability strip may differ from the observed data because pulsations are dampened by convection toward the red edge and the contribution of turbulent pressure at the blue edge. Both boundaries also depend on the chosen value of the mixing length α_{MLT}, a parameter used in time-dependent convection models to create accurate pulsation models. Higher values of α_{MLT} shift the red edge of the instability strip towards hotter stars (Murphy et al. 2020).

The location of TIC 229741985 in relation to the red and blue edge of the instability strip determined in Murphy et al. (2020) is shown in Fig. 2.3 taken from Skarka et al. (2022) marked with the red circle. The studied object lies below the red edge of the theoretical instability strip, but, according to Murphy et al. (2020), pulsators can also be found outside this boundary.

Relation between period and luminosity (P-L relation) can be found when a class of pulsating stars is characterized by a relatively limited range of effective temperatures. Consequently, a significant correlation exists between luminosity and stellar density, associated with the pulsation periods of pressure modes (Ziaali et al. 2019). McNamara (2011) determined a fit to the P-L relation for a sample of radially pulsating δ Scuti stars:

$$M_{\mathrm{V}} = (-2.89 \pm 0.13) \log P - (1.31 \pm 0.10), \tag{4.7}$$

where P is the period of pulsations and M_V is the absolute magnitude in the V photometric filter. Another fit to the P-L relation was determined by Ziaali et al. (2019) on a larger sample of δ Scuti pulsators:

$$M_V = (-2.94 \pm 0.06) \log P - (1.34 \pm 0.06). \tag{4.8}$$

The graph in Fig. 4.7 compares the relation from McNamara (2011) (dashed green line) and the relation determined by Ziaali et al. (2019) (solid black line). From the period of TIC 229741985 light variations P_{f_0}, I have determined the value of absolute magnitude $M_{V\text{teor}} = 1.78(9)$ mag from eq. 4.8 observed for a star with this pulsation period. To compare the theoretical value with the observed, I converted the corrected magnitudes in the G filter to magnitude in the Johnson-Cousin photometric filter V using the relation (Gaia Collaboration et al. 2022):

$$V = 0.02704 - 0.01424(BP - RP) + 0.2156(BP - RP)^2 - 0.01426(BP - RP)^3 + G. \tag{4.9}$$

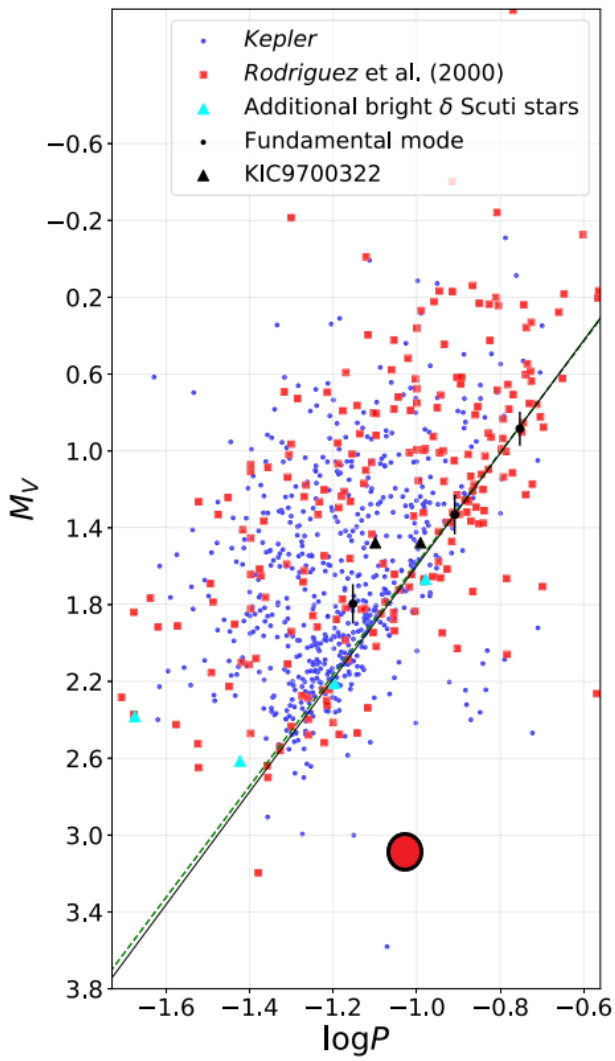

Figure 4.7: Comparison of P-L relations from McNamara (2011) (dashed green line) and Ziaali et al. (2019) (solid black line). Different symbols represent stars from various sources, used to fit the P-L relation from Ziaali et al. (2019). The big red dot represents the location of TIC 229741985.

The observed absolute magnitude in V filter $M_{\mathrm{V}} = 3.090(8)$ mag is almost two times the theoretical magnitude M_{Vteor} and therefore I can conclude, that the pulsations of TIC 229741985 are not following the δ Scuti relation. Fig. 4.7 displays the position of the studied object depending on the P-L relations for the δ Scuti pulsators and shows that observed variations do not satisfy the determined relations. The P-L relations for δ Scuti variables described in McNamara (2011) and Ziaali et al. (2019) are determined only for pulsations in the fundamental radial mode. One of the possible explanations why TIC 229741985 does not follow the P-L relation is that the strongest pulsations in the star are excited in higher radial and non-radial modes, or the nature of the light variations is not in pulsations.

4.4 Binary Hypothesis

In this section, I will present data relevant to the binary hypothesis and verify the system's existence from photometric and spectroscopic observations and data from the Gaia Archive. Using the period $P_{\mathrm{f_0}/2}$, I have constructed a phase diagram of TIC 229741985 for all pipelines. Individual phase diagrams have been binned for clarity; Fig. 4.8 shows the relation between the binned data and the phased plot in the SPOC pipeline, and Fig. 4.9 compares the binned data in different pipelines. By examining the shape of the data phase-folded with $P_{f_0/2}$ and comparing it to the example light curves of binary contact systems displayed in Fig. 1.3, it seems that the studied object shows typical signs of W UMa binary systems.

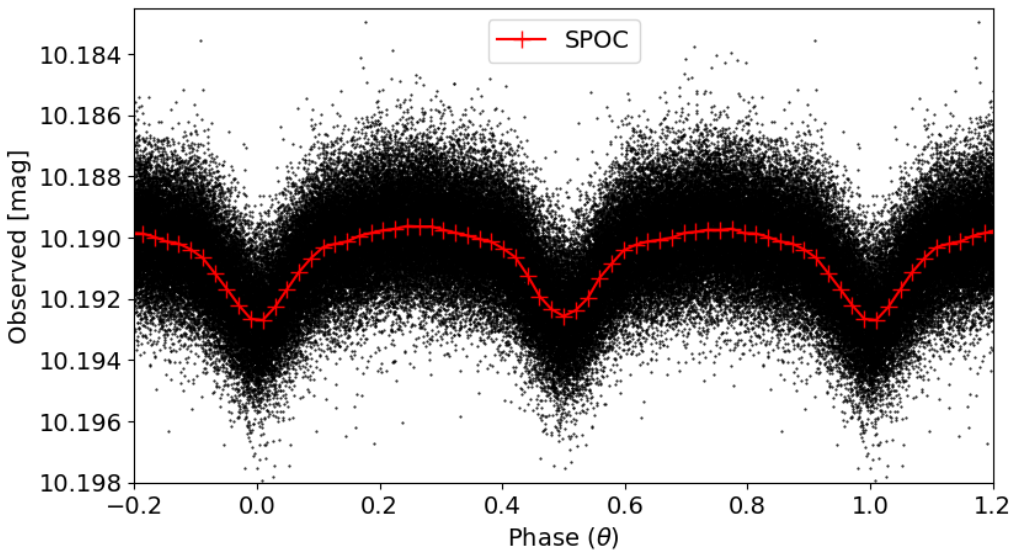

Figure 4.8: Phase diagram with binned data plotted over the light curve in SPOC.

According to Rucinski (1992), the orbital period distribution of contact binaries exhibits a distinct boundary at around 0.22 d, with only a few systems with periods below this threshold. Since then, multiple sky surveys have discovered many eclipsing binary systems in the galactic bulge with short periods with light curves similar to the W UMa stars. Binary systems with periods below the 0.22 d threshold exist and were also detected by Soszyński et al. (2015). Soszyński et al. (2016) analyzed a large number of eclipsing and ellipsoidal binary systems with periods ranging from 0.05 d to over 2600 d and a wide range of variability amplitudes from milimagnitudes to light variations in the order of magnitudes. Fig. 4.10 shows the period distribution of their sample in the

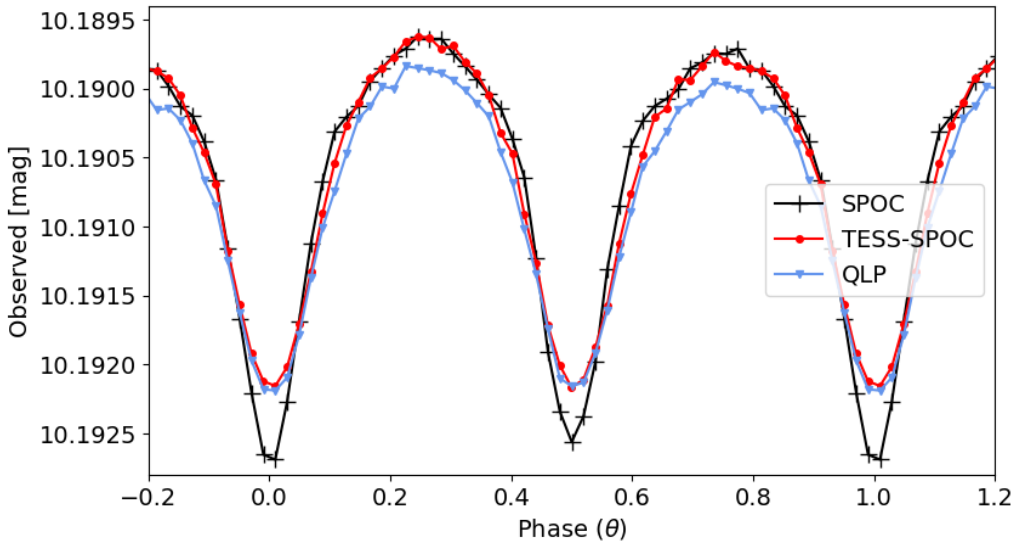

Figure 4.9: Phase diagram of binned TIC 229741985 data showing one orbital cycle in SPOC, TESS-SPOC, and QLP pipelines.

linear scale (the first plot) and logarithmic scale (the second plot). The graph shows a maximum at 0.4 d and the limit for the orbital periods at 0.22 d.

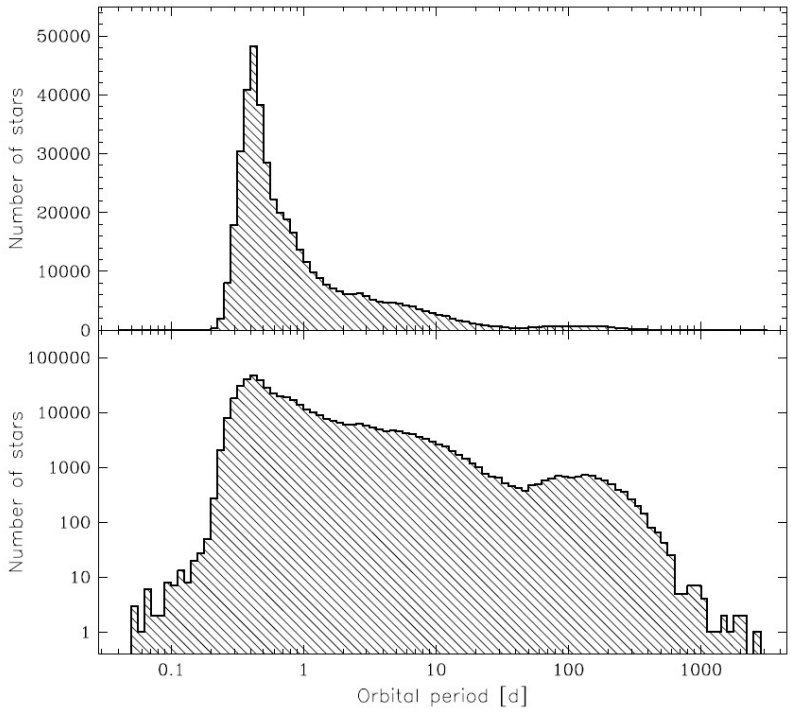

Figure 4.10: Orbital period distribution for binary systems analyzed in Soszyński et al. (2016).

Several hypotheses explain the scarcity of short-period contact binary systems. A system with two low-mass components detached in the beginning would not have time to fill out its Roche lobes within the lifespan of the Universe. However, the existence of such systems may indicate

shorter periods at their birth or high angular momentum loss during the formation process from the protostellar cloud. Jiang et al. (2012) stated that the orbital period limit is caused by the stable mass transfer between the individual components in a binary contact system with the initial primary mass higher than $0.63\,\mathrm{M}_\odot$. Below this limit, the mass transfer becomes unstable, which leads to the formation of a common envelope and the eventual merging of components. Under exceptional circumstances, the Kozai cycles with tidal friction (KCTF) mechanism can shrink the periods of contact binaries and reach the 0.22 d limit (Fabrycky & Tremaine 2007). KCFT mechanism works in a binary system with a third component that induces strong oscillations of eccentricity and, combined with tidal friction, reduces the orbital period of the binary stars. The existence of binary systems with short orbital periods brings new challenges for the theory of the evolution of binary stars; therefore, it is important to identify other objects that could contribute to this sample.

Parameters of TIC 229741985 corresponding to the binary hypothesis are listed in table 4.2 in the 'Binary star hypothesis' column. These values do not correspond with those found in the TIC catalog, as discussed in the previous section. The calculated major axis a is only $0.3\,\mathrm{R}_\odot$ greater than the radii of stars, which means that the major axis is smaller than the sum of radii of individual components. The second component would need to orbit inside the primary star for the system to exist, which is impossible and rules out the binary hypothesis.

Another possibility to theoretically rule out the binary star hypothesis is calculating the critical period. Soszyński et al. (2015) suggested a relation that calculates the critical period of a system, where both components have equal mass M and radii R and fill their Roche lobes. For a system to exist, the orbital period has to be higher than the critical period:

$$P > P_{\mathrm{crit}} = 0.174\sqrt{\frac{R^3}{M}}. \tag{4.10}$$

For TIC 229741985 assuming the parameters in column 'Binary hypothesis' in the table 4.2, the critical period would be $P_{\mathrm{crit}} = 0.259(24)\,\mathrm{d}^{-1}$ which is higher than the orbital period $P_{\mathrm{f_0/2}}$. The components in a binary system with these parameters orbit inside each other. Therefore, the binary explanation of the light variations of TIC 229741985 seems highly unlikely.

Radial Velocities

In the previous section, I argued why the binary hypothesis is not valid for the observed system based on parameters calculated from catalog data and determined period of light variations. It is necessary to independently confirm the binary hypothesis through radial velocity measurements in case of an error in the data from the catalogs, in which case the calculations would be wrong.

The spectral analysis of TIC 229741985 aimed to observe a shift in spectral lines caused by two orbiting stars. Similar luminosity is assumed for the individual components of the studied system; therefore, the Doppler shift should be observable in the spectra, and the lines of both stars would be of similar depth. I calculated the value of semi-amplitude of radial velocities $K = (409 \pm 10)\,\mathrm{kms}^{-1}$ from TIC 229741985 parameters in table 4.2 using a relation:

$$K = \frac{2\pi a \sin i}{P(1-e^2)^{1/2}}, \tag{4.11}$$

where I assumed the system's inclination to be $i = 90°$and circular orbits $e = 0$.

Calculating radial velocities involves determining the displacement of spectral lines caused by the motion of the source either towards or away from the observer. In a binary system, the components move in different directions; while the first moves toward the observer and its spectral lines are blue-shifted, the second component moves away, resulting in a red-shift. In a system

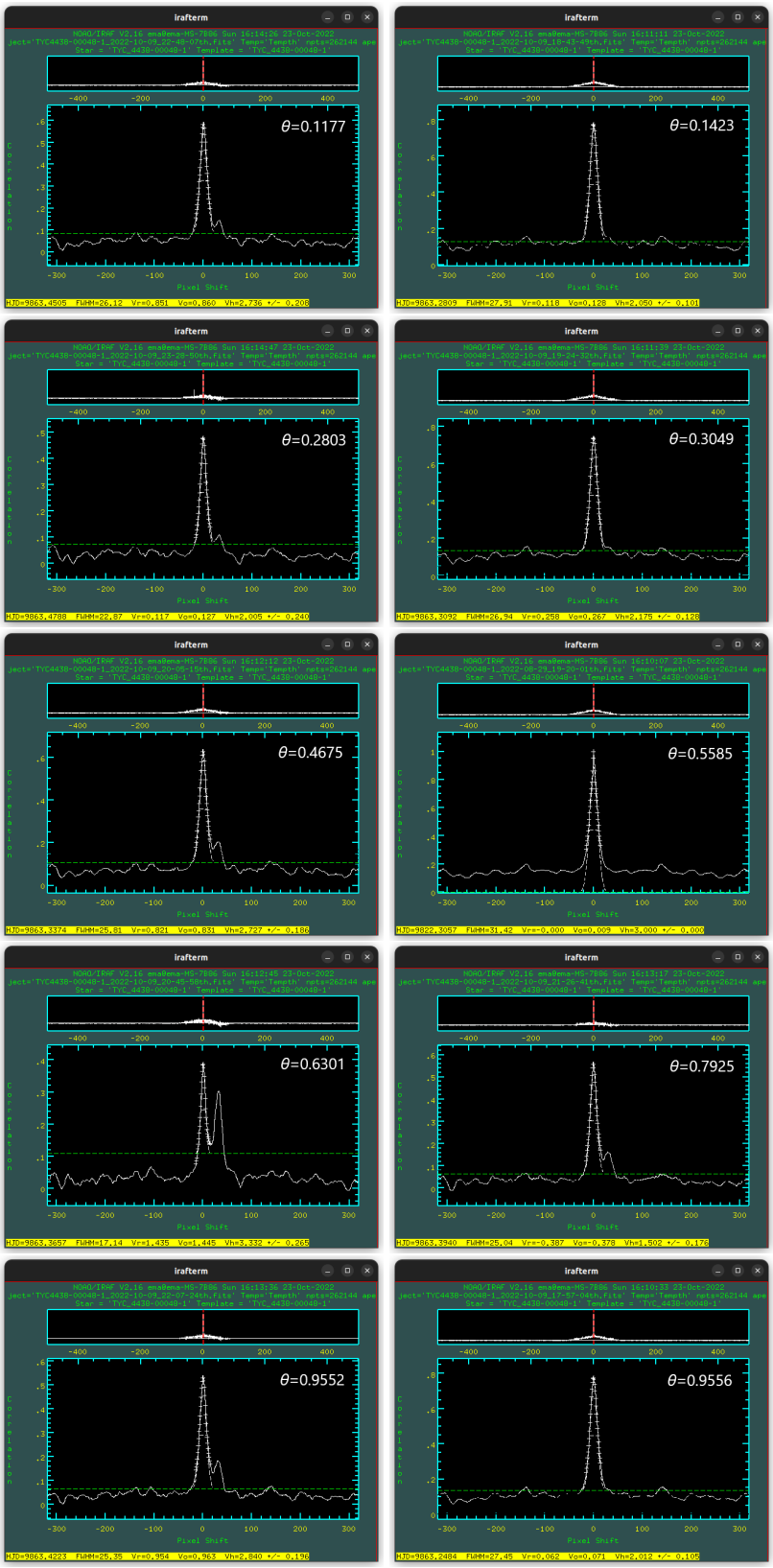

Figure 4.11: Cross-correlation plots of TIC 229741985.

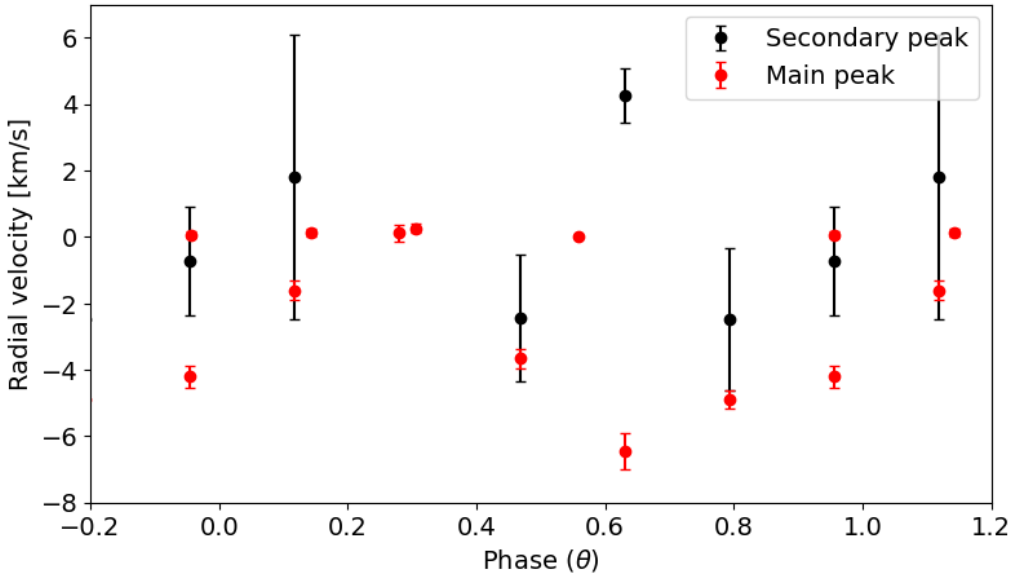

Figure 4.12: Radial velocities of a main and secondary peak in cross-correlation plot.

with similarly luminous components, the constructed radial velocity curve would show the radial velocities of both components in antiphase with identical periods.

Before calculating radial velocities, telluric and heliocentric corrections must be applied to get the most accurate value for radial velocity measurements with `dopcor` task in IRAF. The relative radial velocity calculations were made by cross-correlating the other spectra against a chosen template (in this case, the spectrum from August was chosen because of its high SNR) in a range of 4900-5800 Å (task `fxcor`). The presence of a second peak in the cross-correlation plots can indicate a presence of a second companion. Figures showing the cross-correlation plots of TIC 229741985 spectra are shown in Fig. 4.11. The secondary peak is visible only in a few spectra and does not correspond with the expected phases. In addition, the second peak is always to the right of the dominant peak. It has a significantly lower amplitude than the dominant peak, which does not correspond with the expectations (two peaks with similar amplitudes). The nature of the peak is unclear.

Using IRAF, I calculated relative radial velocities for the main and secondary peaks in the cross-correlation plots, which I compared in Fig. 4.12. The graph shows phased radial velocities across the orbital period $P_{f_0/2}$ with their respective error bars. The time of the first minimum was determined as $t_0 = 24\,571\,790.74\,\mathrm{d}$. Radial velocity curves do not show periodic changes in the gathered data, and the amplitudes of these curves do not reach the calculated range. It is safe to assume that despite less than satisfactory observational conditions, the studied object is not composed of two orbiting stars.

4.5 Third Light Hypothesis

The third light hypothesis assumes an eclipsing binary and a third component that significantly contributes to the overall observed brightness and effectively decreases the amplitude of light variations. In this section, I investigate the possibility of a triple system with a main-sequence component with an eclipsing binary consisting of degenerate components.

From the period $P_{f_0/2}$ of light variations, it is possible to calculate the ratio R^3/M, assuming the observed orbital period of the contact binary is critical. When I calculated the ratio for stars of various spectral types (eq. 4.10) using their typical mass and radius [E10], I discovered that the resulting value $R^3/M \approx 1$ was possible only for solar-like stars. However, a contact system with these parameters cannot exist since the semi-major axis is smaller than the sum of radii of individual components, and the stars would need to orbit inside each other. On the other hand, if it was a system of solar-like stars, both components would be visible in the spectrum, and it could explain the second peak in cross-correlation plots.

Because of the similar depth of minima and continuous light variations, both binary system components would have to have similar luminosities, masses, and radii. The only option to solve the critical period issue is to assume degenerate stars in a short-period system. Keller et al. (2022) studied several eclipsing systems composed of two white dwarf stars with orbital periods up to 2.4 h. In my investigation, I can therefore assume that the eclipsing binary is composed of detached white dwarf stars in a system where the third body outshines the binary system. The dwarf stars are not observable, and the detected light variations result from their eclipses. The calculated parameters for the single-star hypothesis of TIC 229741985 displayed in table 4.2 suggest that the object we observe (the third body) is a main sequence star slightly larger than the Sun.

Fig. 4.13 shows the HR diagram of a great number of objects observed by the Gaia mission [E11]. The third body in the studied system is a main sequence star with an absolute magnitude observed in G band $M_G = 3.008(8)$ mag. The eclipsing binary composed of two white dwarf stars with similar luminosities has the amplitude of light variations $\Delta m_{WD} = 0.753$ mag in case of a total eclipse. We do not observe total eclipses, which means that the system's inclination is not $i = 90°$, and the observed amplitude of light variations would be lower than the value I specified. The presence of a third light in this system decreases the amplitude even more.

Using Pogson's equation, I calculated the theoretical magnitude difference from the observed amplitude of light variations $\Delta m = 0.003$ mag assuming the highest possible amplitude 0.753 mag, derived from Fig. 4.9, between moments when all three system components were visible and when only the main sequence star and one dwarf were visible due to eclipses. The magnitude difference between the components of the eclipsing binary and the third body would be $\Delta M_{teor} = 6.4$ mag to yield such amplitudes. However, when looking at the HR diagram, this would mean that the components of the eclipsing binary would be white dwarfs with absolute magnitude around the value of 10 mag or brighter, which is a very sparsely covered region. The amplitude of the system would be even smaller due to an inclination angle other than 90°, and the magnitude difference between the components would have to be smaller to reach 0.003 mag. The white dwarves then move to an even more sparsely covered region of HRD. It is highly unlikely that TIC 229741985 is a system in such a configuration.

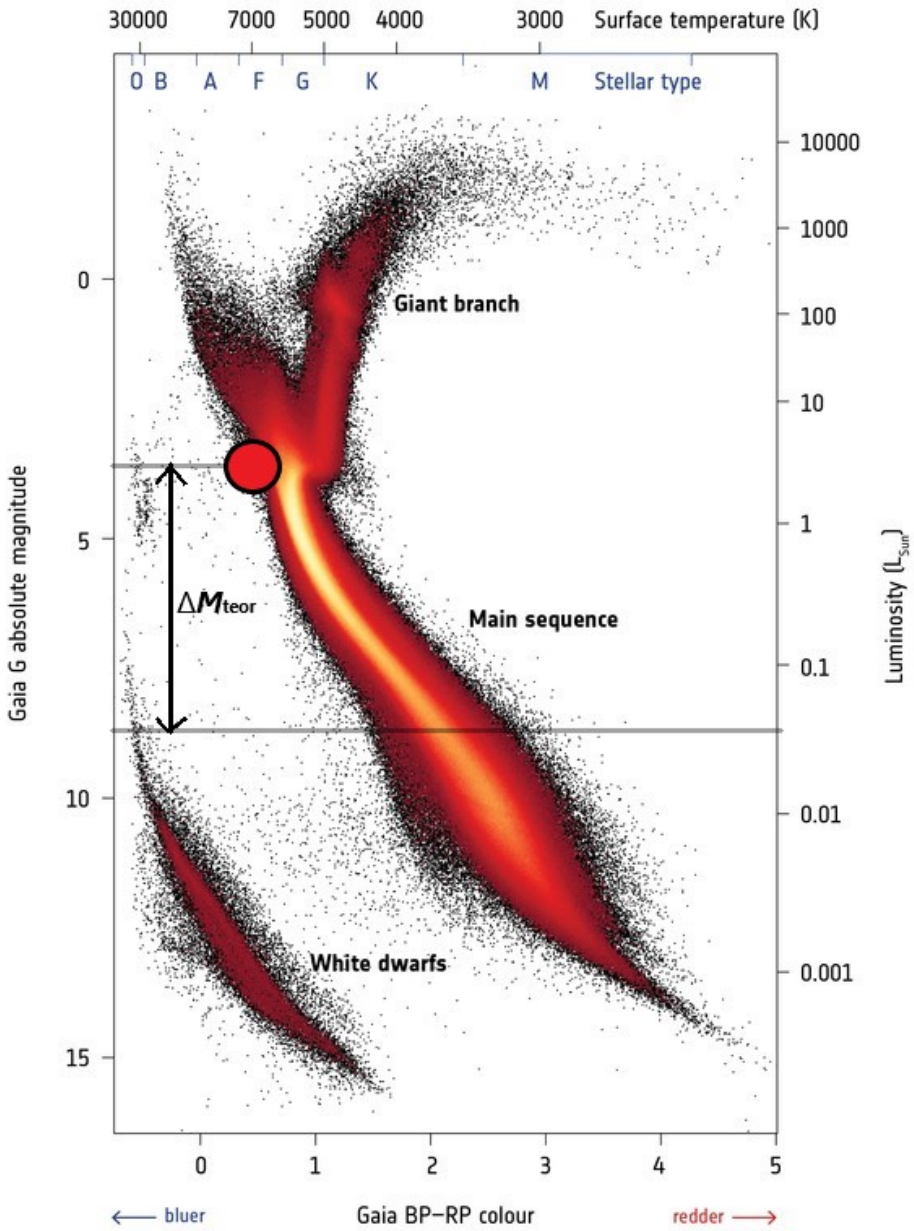

Figure 4.13: Hertzsprung-Russell diagram containing stars from the second data release of the Gaia satellite. The red circle represents an approximate location of TIC 229741985 on the HR diagram. ΔM_{teor} is the calculated magnitude difference between the third body and an eclipsing system that yields amplitudes of light variations which correspond with the observed amplitudes. Copyright: ESAGaiaDPAC, CC BY-SA 3.0 IGO.

Conclusion

This thesis aimed to reveal the mechanism responsible for observed light variations and describe the respective parameters of TIC 229741985. The period of light changes fell within the range of typical δ Scuti pulsators, while the shape of the light curve constructed using double this period resembled that of W UMa binary light curves. Data from various catalogs and photometric and spectroscopic observations were used to investigate the nature of light variations and classify the studied object.

The analysis of TIC 229741985 was performed on photometric data collected from the TESS mission using the LIGHTKURVE package in Python and PERIOD04 - a software for time series analysis. Additional information was extracted from 11 spectra taken with the Ondřejov Echelle Spectrograph reduced and processed with IRAF. Supplementary photometric data from Kraví Hora and Vyškov observatory aimed to measure the amplitude difference between blue and red photometric filters to better describe the nature of variations. However, due to the low amplitude and poor observing conditions, these data were inconclusive and were not used further in the work.

Chapter 4 describes various hypotheses explaining the origin of TIC 229741985 variability. The first hypothesis assumes the object to be a δ Scuti pulsator, as its observed period of light variations falls within the typical range for this class of objects. δ Scuti pulsators lie in the intersection of the main sequence and the instability strip and follow well-defined period-luminosity relation for fundamental radial modes. However, it seems that TIC 229741985, if it were a δ Scuti star, does not follow this P-L relation, which can be explained by higher radial and non-radial modes. Alternatively, its variability does not originate in pulsations.

The second hypothesis considers the object a contact binary system with two main-sequence stars with similar masses and radii orbiting each other. However, when I calculated the parameters of this system using the catalog data, the semi-major axis was shorter than the sum of their radii, meaning that one component would need to orbit inside the other. Additionally, the observed period was lower than the critical period of the contact system. Therefore, I can conclude that a system containing two main-sequence stars with these parameters cannot exist. The binary hypothesis needed to be verified through the spectroscopic measurement of radial velocities in case of an error in the catalog data, but no variations in radial velocity were observed. This makes the binary hypothesis not probable.

As the last option, I considered the possibility that a third component in the system contributes to the brightness and effectively decreases the amplitude of light variations caused by a binary system that is significantly fainter than the third component. The third object would be a main-sequence star with parameters corresponding to the single-star hypothesis. The only option to solve this issue with the critical period is for the components of the binary system to be degenerate remnants, for example, white dwarves. However, the calculated magnitude difference between the bright object and the binary system places the white dwarf stars in a sparsely populated area of the HR diagram. The system in this configuration is not very probable. Therefore, I consider this hypothesis as unlike.

In conclusion, the most probable explanation for the light variations of TIC 229741985 is the pulsation hypothesis, where the pulsations are in higher radial or non-radial modes. Further analysis of this object with larger telescopes allowing to get high SNR spectra with better time resolution, will be necessary to make a final decision about the nature of the light variations.

Bibliography

Almeida, A., Anderson, S. F., Argudo-Fernández, M. & et al. (2023), 'The Eighteenth Data Release of the Sloan Digital Sky Surveys: Targeting and First Spectra from SDSS-V', *arXiv e-prints* p. arXiv:2301.07688.

Barclay, T. (2023*a*), 'Lightcurvefile objects'. Online available at: https://heasarc.gsfc.nasa.gov/docs/tess/LightCurveFile-Object-Tutorial.html; accessed at 17/03/2023.

Barclay, T. (2023*b*), 'The primary mission - tess science support centre'. Online available at: https://heasarc.gsfc.nasa.gov/docs/tess/primary.html; accessed at 24/02/2023.

Barclay, T. (2023*c*), 'The second extended mission - tess science support centre'. Online available at: https://heasarc.gsfc.nasa.gov/docs/tess/second-extended.html; accessed at 24/02/2023.

Bonnarel, F., Fernique, P., Bienaymé, O., Egret, D., Genova, F., Louys, M., Ochsenbein, F., Wenger, M. & Bartlett, J. G. (2000), 'The ALADIN interactive sky atlas. A reference tool for identification of astronomical sources', *Astronomy and Astrophysics, Supplement* **143**, 33–40.

Borucki, W. J., Koch, D., Basri, G. & et al. (2010), 'Kepler Planet-Detection Mission: Introduction and First Results', *Science* **327**(5968), 977.

Caldwell, D. A., Tenenbaum, P., Twicken, J. D. & et al. (2020), 'TESS Science Processing Operations Center FFI Target List Products', *Research Notes of the American Astronomical Society* **4**(11), 201.

Catelan, M. & Smith, H. (2015), *Pulsating stars*, Wiley.

Chaffee, F. H., J. & Schroeder, D. J. (1976), 'Astronomical applications of echelle spectroscopy.', *Annual Review of Astronomy and Astrophysics* **14**, 23–42.

CSIRO (n.d.), 'Types of binary stars'. Online available at: https://www.atnf.csiro.au/outreach/education/senior/astrophysics/binary_types.html; accessed at 18/01/2023.

Eyer, L. & Mowlavi, N. (2008), Variable stars across the observational HR diagram, *in* 'Journal of Physics Conference Series', Vol. 118 of *Journal of Physics Conference Series*, p. 012010.

Fabrycky, D. & Tremaine, S. (2007), 'Shrinking Binary and Planetary Orbits by Kozai Cycles with Tidal Friction', *Astrophysical Journal* **669**(2), 1298–1315.

Gaia Collaboration, Eyer, L., Rimoldini, L. & et al. (2019), 'Gaia Data Release 2. Variable stars in the colour-absolute magnitude diagram', *Astronomy and Astrophysics* **623**, A110.

Gaia Collaboration, Prusti, T., de Bruijne, J. H. J. & et al. (2016), 'The Gaia mission', *Astronomy and Astrophysics* **595**, A1.

Gaia Collaboration, Vallenari, A., Brown, A. G. A., Prusti, T. & et al. (2022), 'Gaia Data Release 3: Summary of the content and survey properties', *arXiv e-prints* p. arXiv:2208.00211.

Gangestad, J. W., Henning, G. A., Persinger, R. R. & Ricker, G. R. (2013), 'A High Earth, Lunar Resonant Orbit for Lower Cost Space Science Missions', *arXiv e-prints* p. arXiv:1306.5333.

Hroch, F. (2014), 'Munipack: General astronomical image processing software', Astrophysics Source Code Library, record ascl:1402.006.

Huang, C. X., Vanderburg, A., Pál, A. & et al. (2020*a*), 'Photometry of 10 Million Stars from the First Two Years of TESS Full Frame Images: Part I', *Research Notes of the American Astronomical Society* **4**(11), 204.

Huang, C. X., Vanderburg, A., Pál, A. & et al. (2020*b*), 'Photometry of 10 Million Stars from the First Two Years of TESS Full Frame Images: Part II', *Research Notes of the American Astronomical Society* **4**(11), 206.

Jenkins, J. M. (2015), Overview of the TESS Science Pipeline, *in* 'AAS/Division for Extreme Solar Systems Abstracts', Vol. 47 of *AAS/Division for Extreme Solar Systems Abstracts*, p. 106.05.

Jiang, D., Han, Z., Ge, H., Yang, L. & Li, L. (2012), 'The short-period limit of contact binaries', *Monthly Notices of the RAS* **421**(4), 2769–2773.

Jordi, C., Gebran, M., Carrasco, J. M. & et al. (2010), 'Gaia broad band photometry', *Astronomy and Astrophysics* **523**, A48.

Kabáth, P., Skarka, M., Sabotta, S. & et al. (2020), 'Ondřejov Echelle Spectrograph, Ground Based Support Facility for Exoplanet Missions', *Publications of the Astronomical Society of the Pacific* **132**(1009), 035002.

Kamilla, S., Roy, G., Nayak, M., Khamari Sharma, N. & et al. (2011), 'Binary star system- a spectral analysis', *LATIN AMERICAN JOURNAL OF PHYSICS* **5**.

Keesey, L. (2017), 'New explorer mission chooses the 'just-right' orbit'. Online available at: https://www.nasa.gov/content/goddard/new-explorer-mission-chooses-the-just-right-orbit; accessed at 15/02/2023.

Keller, P. M., Breedt, E., Hodgkin, S., Belokurov, V., Wild, J., García-Soriano, I. & Wise, J. L. (2022), 'Eclipsing white dwarf binaries in Gaia and the Zwicky Transient Faaccility', *Monthly Notices of the RAS* **509**(3), 4171–4188.

Kopal, Z. (1955), 'The classification of close binary systems', *Annales d'Astrophysique* **18**, 379.

Koubský, P., Mayer, P., Čáp, J. & et al. (2004), 'Ondřejov Echelle Spectrograph - OES', *Publications of the Astronomical Institute of the Czechoslovak Academy of Sciences* **92**, 37–43.

Kunimoto, M., Huang, C., Tey, E. & et al. (2021), 'Quick-look Pipeline Lightcurves for 9.1 Million Stars Observed over the First Year of the TESS Extended Mission', *Research Notes of the American Astronomical Society* **5**(10), 234.

Kunimoto, M., Tey, E., Fong, W. & et al. (2022), 'Quick-look Pipeline Light Curves for 5.7 Million Stars Observed Over the Second Year of TESS' First Extended Mission', *Research Notes of the American Astronomical Society* **6**(11), 236.

Kurtz, D. W. (2006), 'Stellar pulsation: an overview', *Communications in Asteroseismology* **147**, 6–30.

Lenz, P. & Breger, M. (2005), 'Period04 User Guide', *Communications in Asteroseismology* **146**, 53–136.

Lightkurve Collaboration, Cardoso, J. V. d. M., Hedges, C. & et al. (2018), 'Lightkurve: Kepler and TESS time series analysis in Python', Astrophysics Source Code Library.

Malatesta, K. (n.d.), 'W ursae majoris'. Online available at: https://www.aavso.org/vsots_wuma; accessed at 21/01/2023.

McNamara, D. H. (2011), 'Delta Scuti, SX Phoenicis, and RR Lyrae Stars in Galaxies and Globular Clusters', *Astronomical Journal* **142**(4), 110.

Mikulášek, Z., Papoušek, J., Tremko, J. & Vetešník, M. (2000), 'Atmospheric extinction at the Brno and Skalnate Pleso Observatories I. Instrumentation, observations and review of data', *Contributions of the Astronomical Observatory Skalnate Pleso* **30**(2), 89–98.

Mikulášek, Z. & Krtička, J. (2005), *Základy fyziky hvězd*, Masaryk University.

Mikulášek, Z. & Zejda, M. (2013), *Úvod do studia proměnných hvězd*, Masaryk University.

MIT, T. (n.d.), 'Tess observations'. Online available at: https://tess.mit.edu/observations/; accessed at 25/02/2023.

Murphy, S. J., Saio, H., Takada-Hidai, M. & et al. (2020), 'On the first δ Sct-roAp hybrid pulsator and the stability of p and g modes in chemically peculiar A/F stars', *Monthly Notices of the RAS* **498**(3), 4272–4286.

Paegert, M., Stassun, K., Collins, K. & et al. (2022), 'Tess input catalog version 8.2 (tic v8.2)'.

Pietrukowicz, P., Soszyński, I., Netzel, H. & et al. (2020), 'Over 10000 δ Scuti Stars toward the Galactic Bulge from OGLE-IV', *Acta Astronomica* **70**(4), 241–263.

Prša, A., Batalha, N., Slawson, R. W. & et al. (2011), 'Kepler Eclipsing Binary Stars. I. Catalog and Principal Characterization of 1879 Eclipsing Binaries in the First Data Release', *Astronomical Journal* **141**(3), 83.

Ricker, G. R., Winn, J. N., Vanderspek, R. & et al. (2015), 'Transiting Exoplanet Survey Satellite (TESS)', *Journal of Astronomical Telescopes, Instruments, and Systems* **1**, 014003.

Rucinski, S. M. (1992), 'Can Full Convection Explain the Observed Short-Period Limit of the W UMa-Type Binaries?', *Astronomical Journal* **103**, 960.

Skarka, M., Žák, J., Fedurco, M., Paunzen, E. & et al. (2022), 'Periodic variable A-F spectral type stars in the northern TESS continuous viewing zone. I. Identification and classification', *Astronomy and Astrophysics* **666**, A142.

Soszyński, I., Pawlak, M., Pietrukowicz, P. & et al. (2016), 'The OGLE Collection of Variable Stars. Over 450 000 Eclipsing and Ellipsoidal Binary Systems Toward the Galactic Bulge', *Acta Astronomica* **66**(4), 405–420.

Soszyński, I., Stepień, K., Pilecki, B. & et al. (2015), 'Ultra-Short-Period Binary Systems in the OGLE Fields Toward the Galactic Bulge', *Acta Astronomica* **65**(1), 39–62.

Stassun, K. G., Oelkers, R. J., Pepper, J. & et al. (2018), 'The TESS Input Catalog and Candidate Target List', *Astronomical Journal* **156**(3), 102.

Tody, D. (1986), The IRAF Data Reduction and Analysis System, *in* D. L. Crawford, ed., 'Instrumentation in astronomy VI', Vol. 627 of *Society of Photo-Optical Instrumentation Engineers (SPIE) Conference Series*, p. 733.

Twicken, J. D., Caldwell, D. A., Jenkins, J. M. & et al. (2020), 'Tess science data products description document: Exp-tess-arc-icd-0014 rev f'. Online available at: https://ntrs.nasa.gov/api/citations/20205008729/downloads/EXP-TESS-ARC-ICD-TM-0014-Rev-F_v2.pdf; accessed at 23/02/2023.

VanderPlas, J. T. (2018), 'Understanding the Lomb-Scargle Periodogram', *Astrophysical Journal, Supplement* **236**(1), 16.

Vanderspek, R., Doty, J. R., Fausnaugh, M., Villasenor, J. N. S. and Berta-Thompson, Z. K., Burke, J. & Ricker, G. R. (2018), 'Technical manual'. Online available at: https://archive.stsci.edu/files/live/sites/mast/files/home/missions-and-data/active-missions/tess/_documents/TESS_Instrument_Handbook_v0.1.pdf; accessed at 13/12/2022.

Verbunt, F. (2015), 'Compact binaries - part i'. Lecture Course, Radboud University.

Škoda, P., Šurlan, B. & Tomić, S. (2008), Investigation of residual blaze functions in slit-based echelle spectrograph, *in* I. S. McLean & M. M. Casali, eds, 'Ground-based and Airborne Instrumentation for Astronomy II', Vol. 7014 of *Society of Photo-Optical Instrumentation Engineers (SPIE) Conference Series*, p. 70145X.

Ziaali, E., Bedding, T. R., Murphy, S. J., Van Reeth, T. & Hey, D. R. (2019), 'The period-luminosity relation for δ Scuti stars using Gaia DR2 parallaxes', *Monthly Notices of the RAS* **486**(3), 4348–4353.

Electronic sources

[E1] accessed 10 February 2023,
https://gea.esac.esa.int/archive/documentation/GDR2/Gaia_archive/chap_datamodel/sec_dm_main_tables/ssec_dm_gaia_source.html

[E2] accessed 10 February 2023, https://gea.esac.esa.int/archive/

[E3] accessed 11 February 2023, http://simbad.cds.unistra.fr/simbad/sim-id?Ident=%40300436&Name=TYC%204438-48-1&submit=submit

[E4] accessed 11 February 2023,
https://www.cosmos.esa.int/web/gaia/edr3-passbands

[E5] accessed 11 February 2023, https://sites.uni.edu/morgans/astro/course/Notes/section2/spectraltemps.html

[E6] accessed 11 February 2023, https://archive.stsci.edu/missions-and-data/tess

[E7] accessed 11 February 2023, https://astro.physics.muni.cz/observatory/

[E8] accessed 11 February 2023,
https://astro.physics.muni.cz/observatory/instrumentation/

[E9] accessed 5 May 2023, https://hvezdarna.zoo-vyskov.cz/historie

[E10] accessed 5 May 2023,
https://stelweb.asu.cas.cz/~nemeth/work/stuff/startype/

[E11] accessed 5 May 2023, https://creativecommons.org/licenses/by-sa/3.0/igo/

Appendix

Pixel maps for SPOC and TESS-SPOC pipelines, containing frequency spectrum of each TPF pixel in a range 0 - 23.5 cd. The aperture mask for TIC 229741985 is highlighted with the red squares in all sectors.

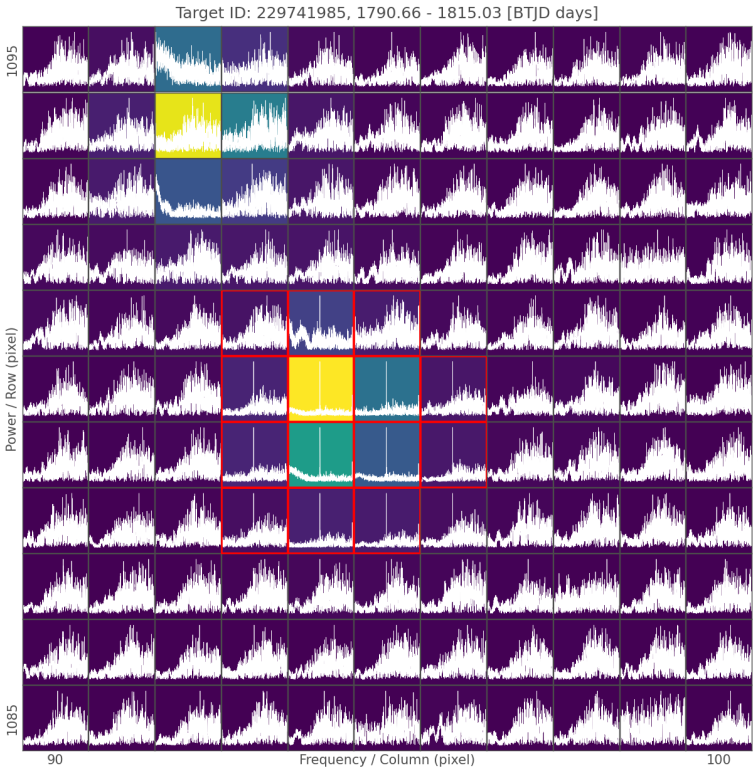

Figure A.1: Pixel map of TIC 229741985 for sector 18 for the SPOC pipeline.

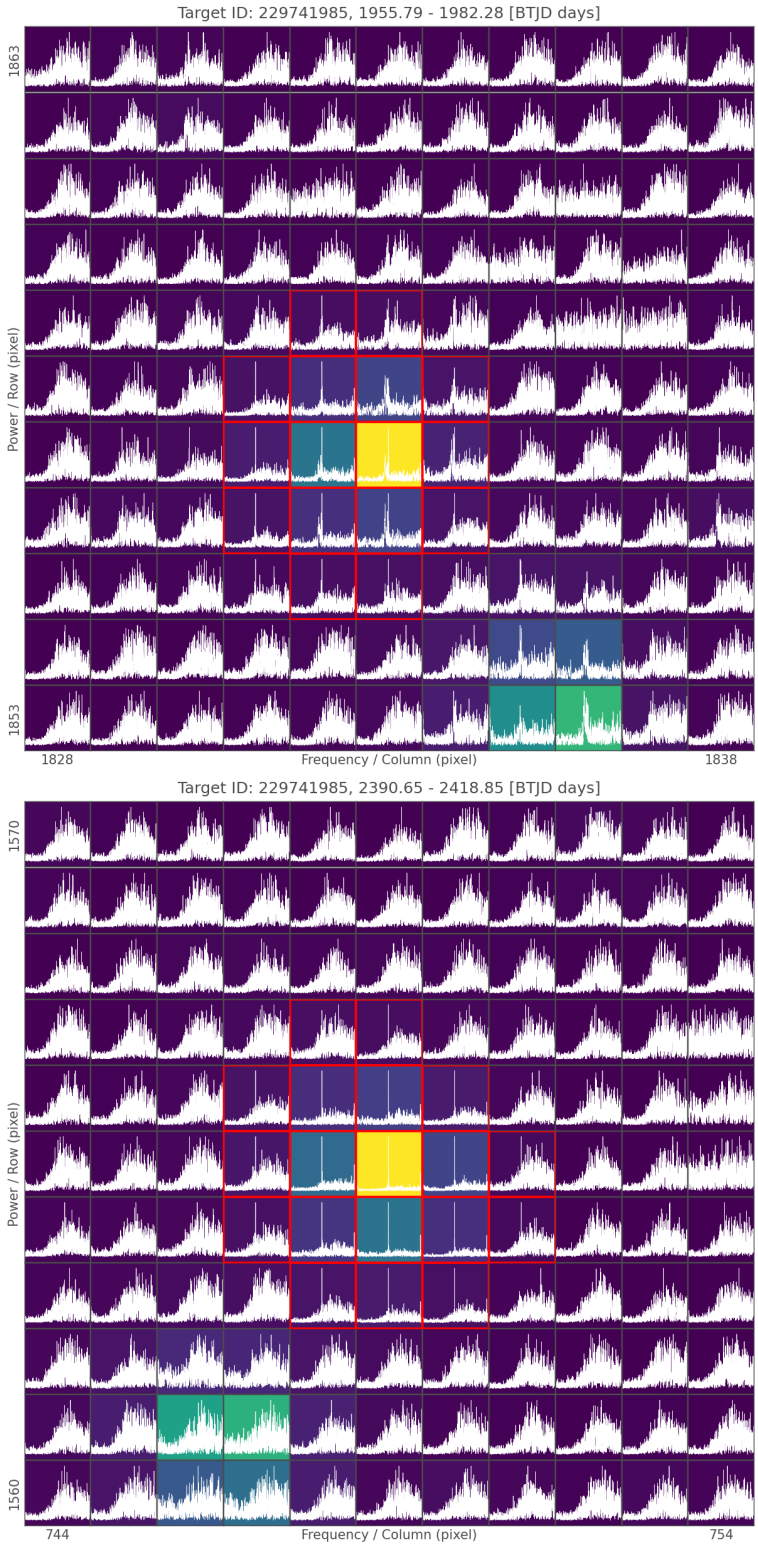

Figure A.2: Pixel map of TIC 229741985 for sector 24 (the first image) and sector 40 (the second image) for the SPOC pipeline.

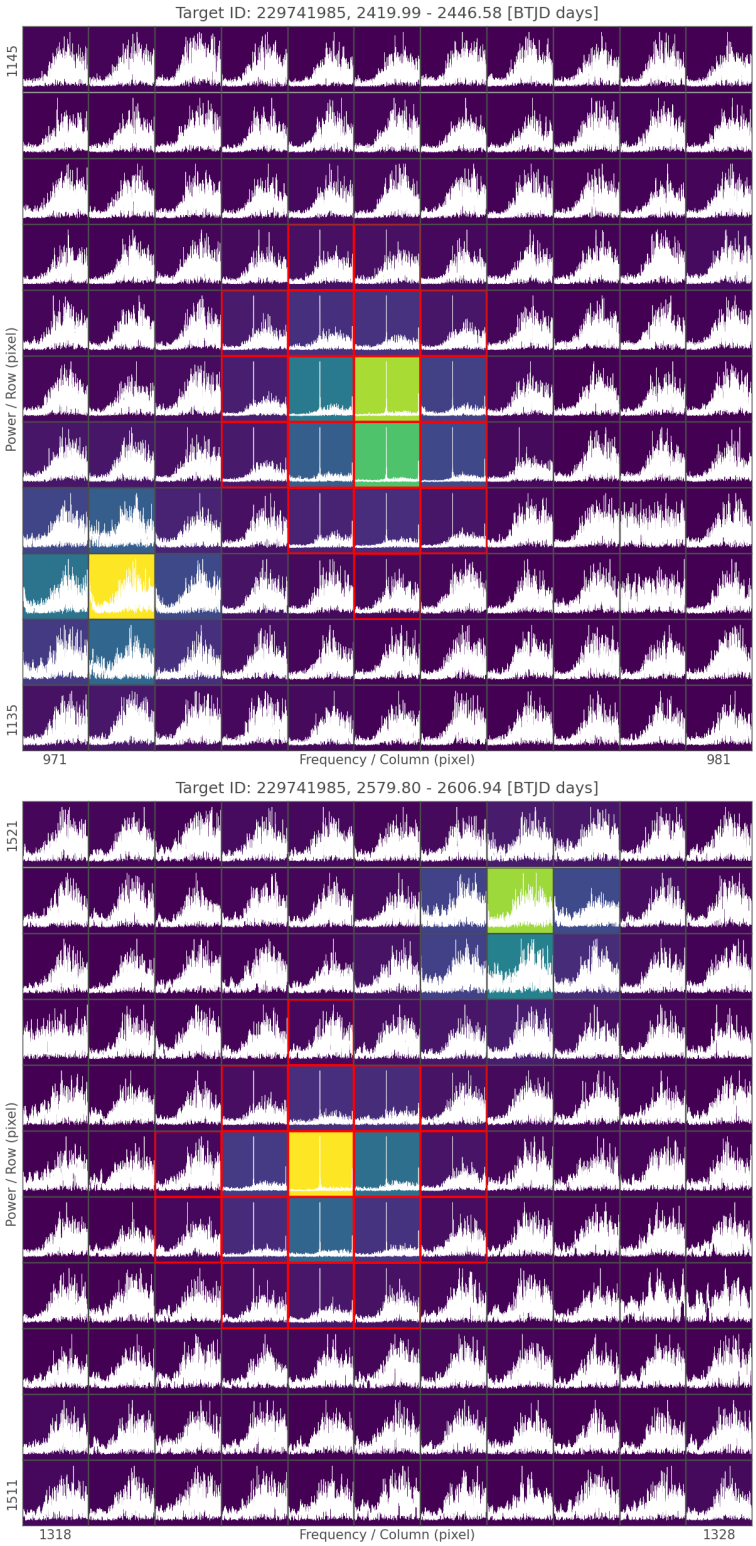

Figure A.3: Pixel map of TIC 229741985 for sector 41 (the first image) and sector 47 (the second image) for the SPOC pipeline.

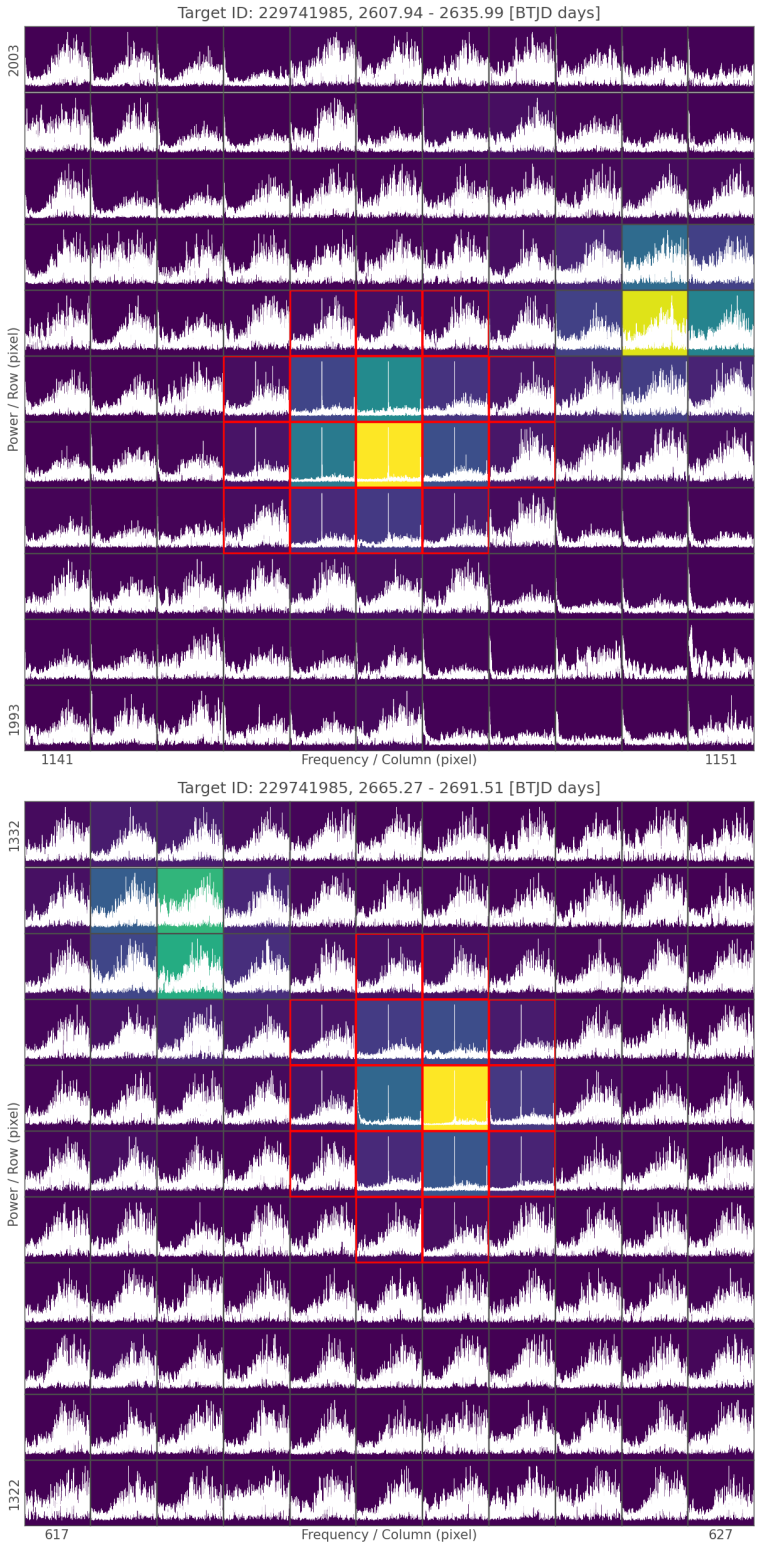

Figure A.4: Pixel map of TIC 229741985 for sector 48 (the first image) and sector 50 (the second image) for the SPOC pipeline.

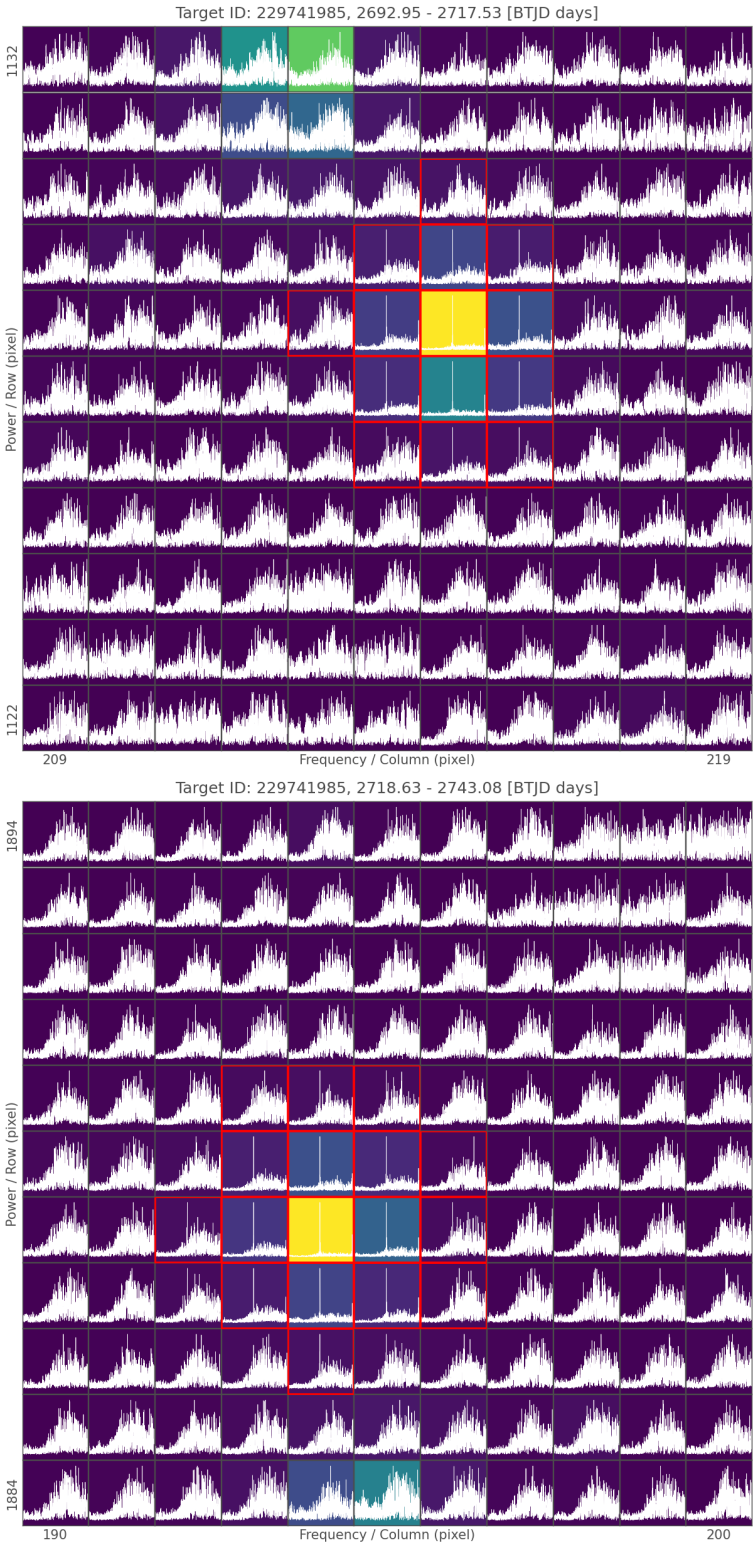

Figure A.5: Pixel map of TIC 229741985 for sector 51 (the first image) and sector 52 (the second image) for the SPOC pipeline.

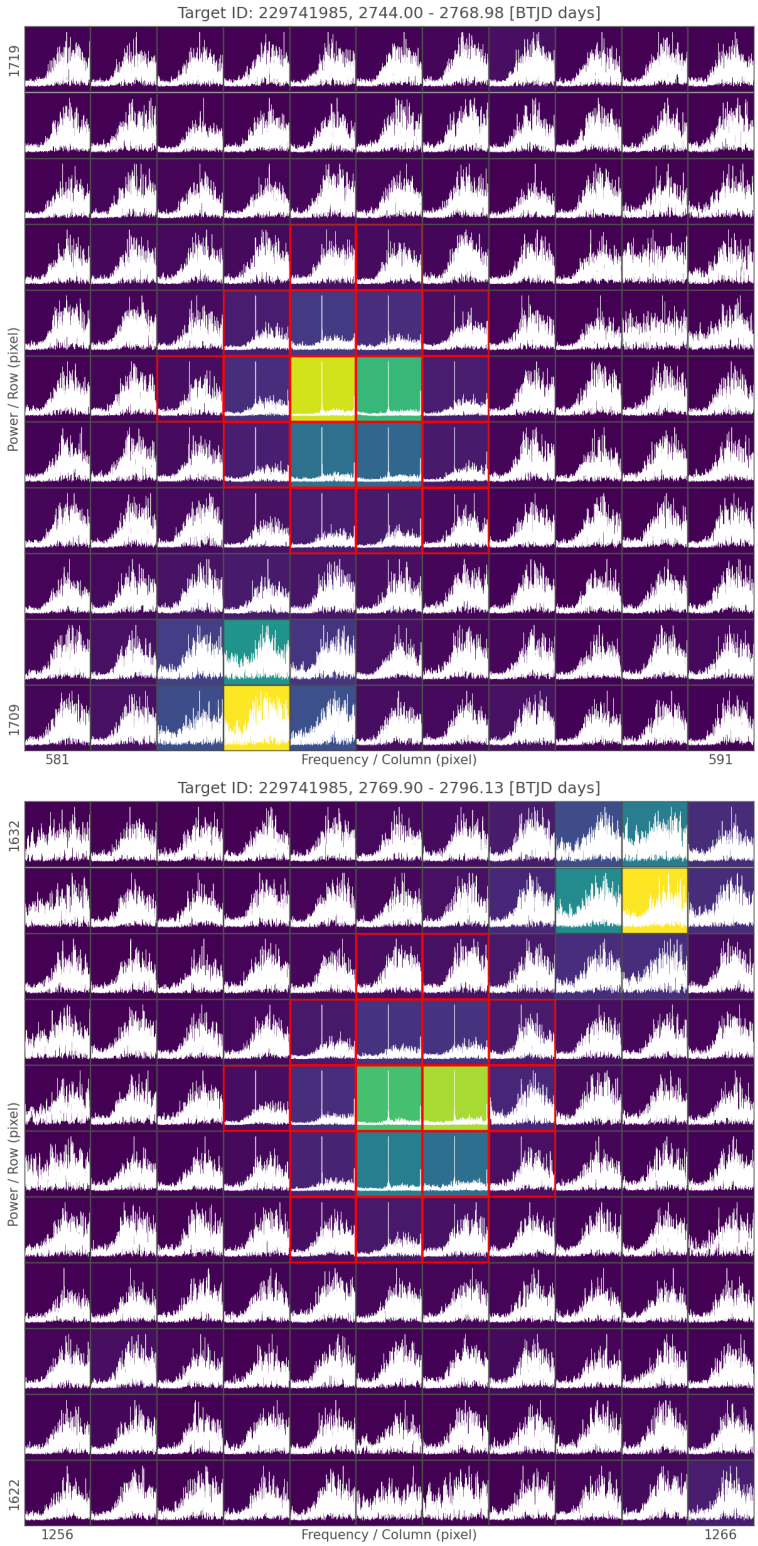

Figure A.6: Pixel map of TIC 229741985 for sector 53 (the first image) and sector 54 (the second image) for the SPOC pipeline.

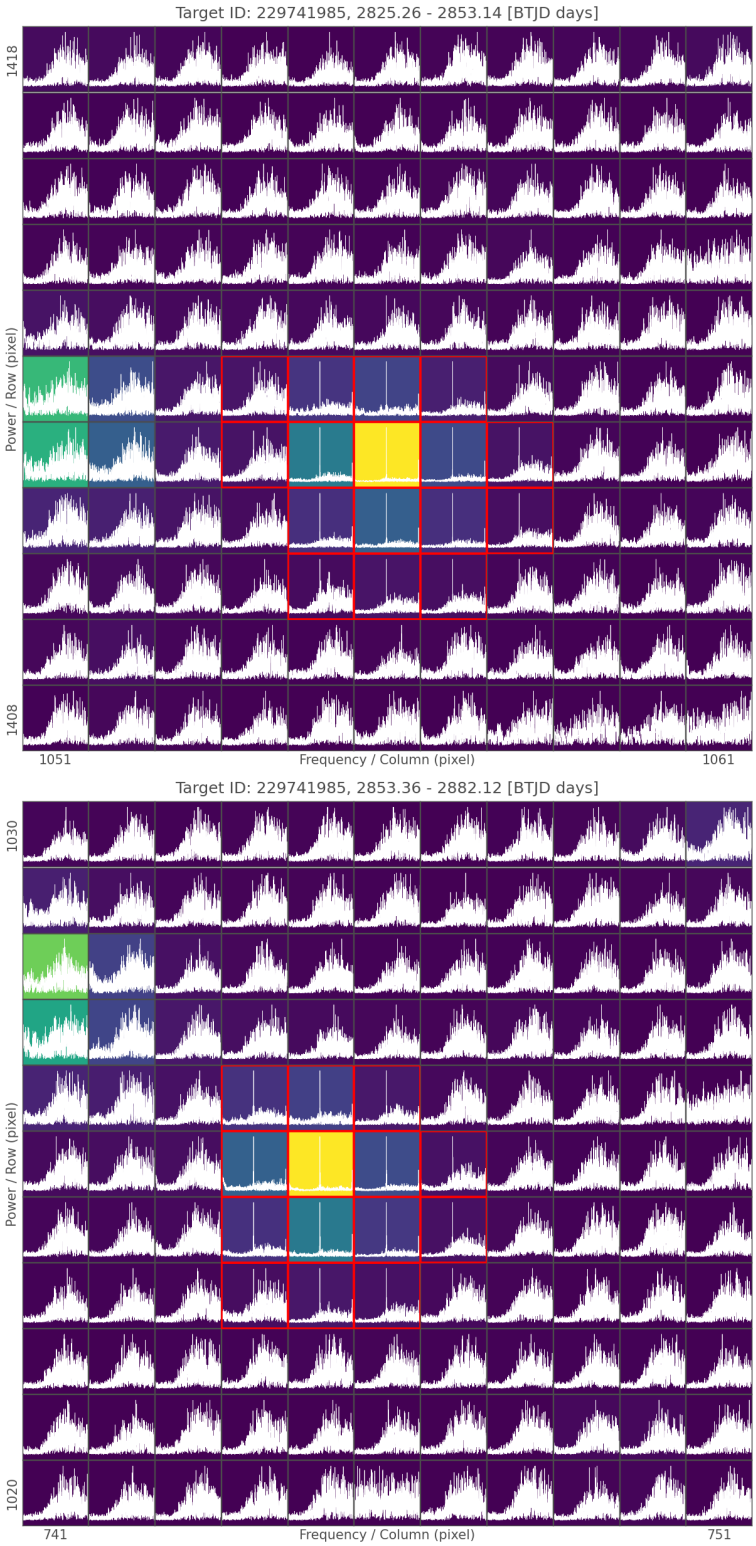

Figure A.7: Pixel map of TIC 229741985 for sector 56 (the first image) and sector 57 (the second image) for the SPOC pipeline.

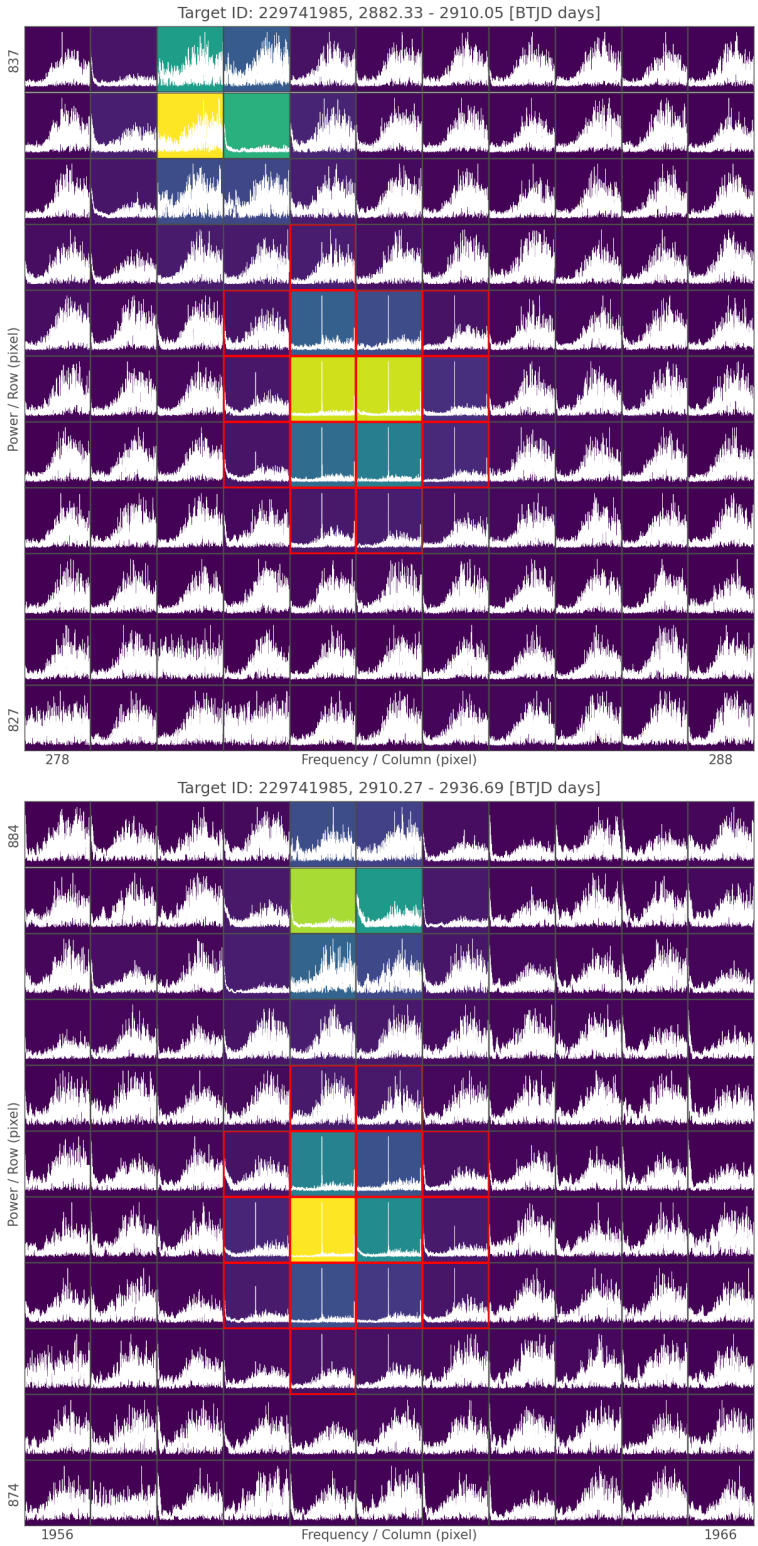

Figure A.8: Pixel map of TIC 229741985 for sector 58 (the first image) and sector 59 (the second image) for the SPOC pipeline.

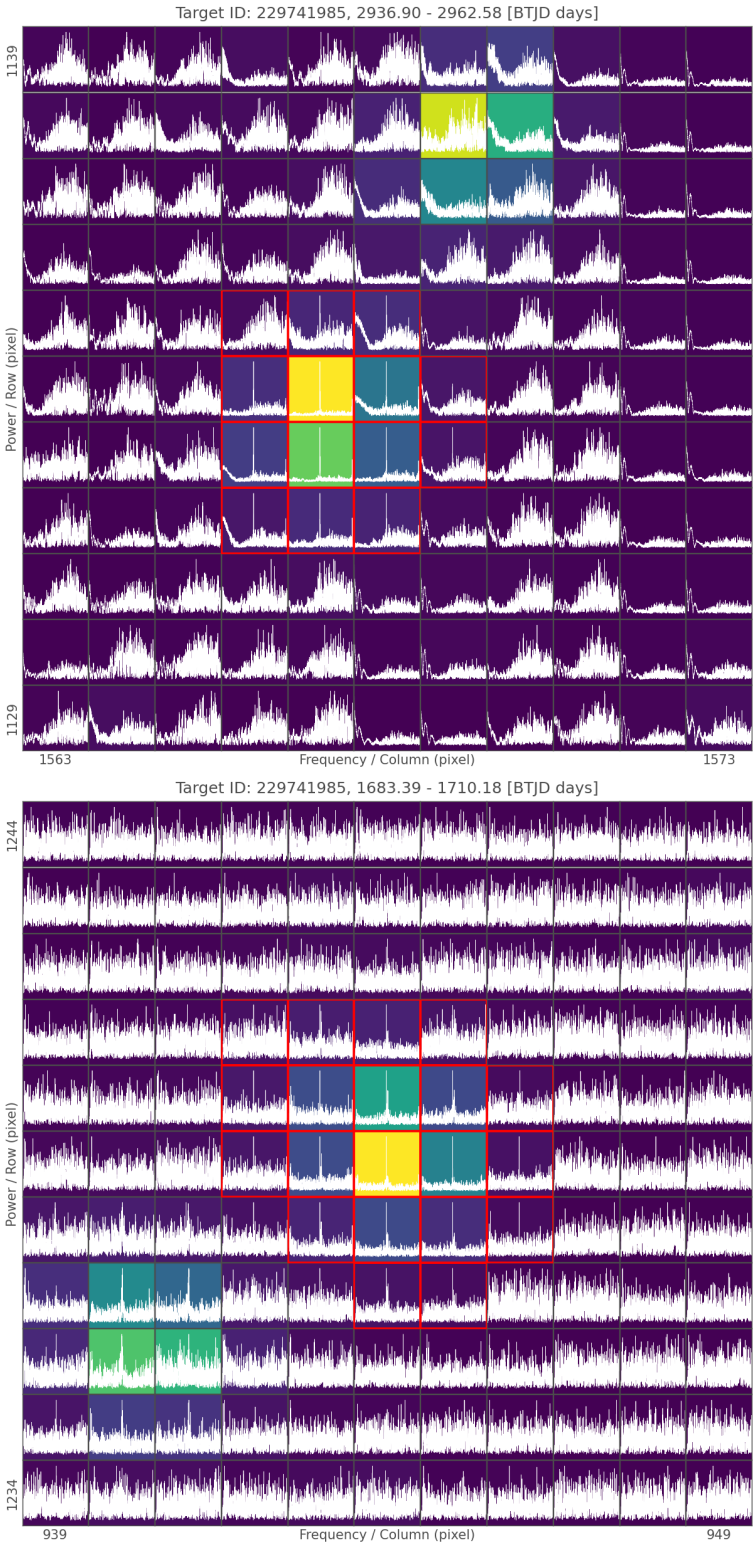

Figure A.9: Pixel map of TIC 229741985 for sector 60 (the first image) for the SPOC pipeline and sector 14 (the second image) for the TESS-SPOC pipeline.

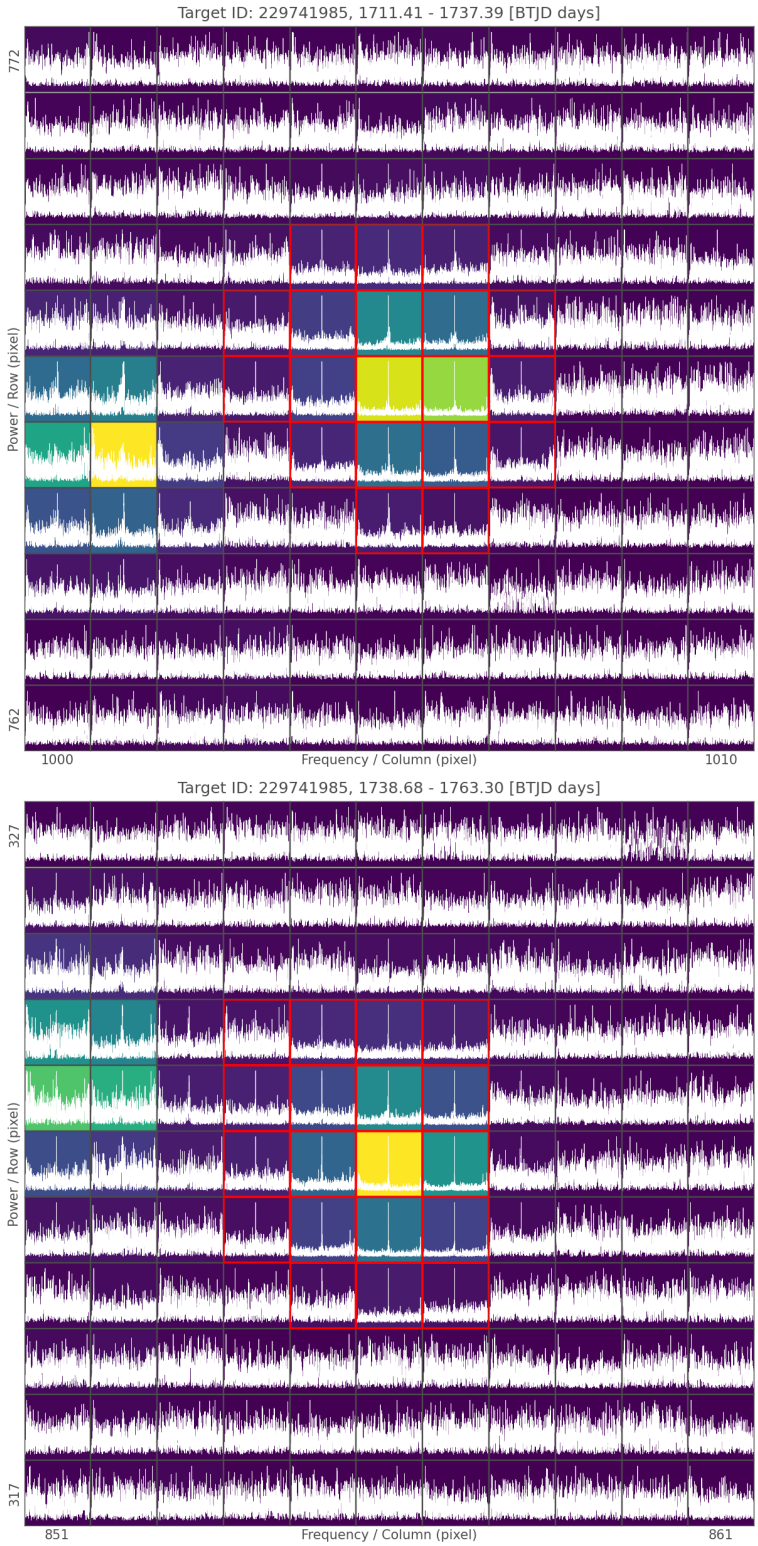

Figure A.10: Pixel map of TIC 229741985 for sector 15 (the first image) and sector 16 (the second image) for the TESS-SPOC pipeline.

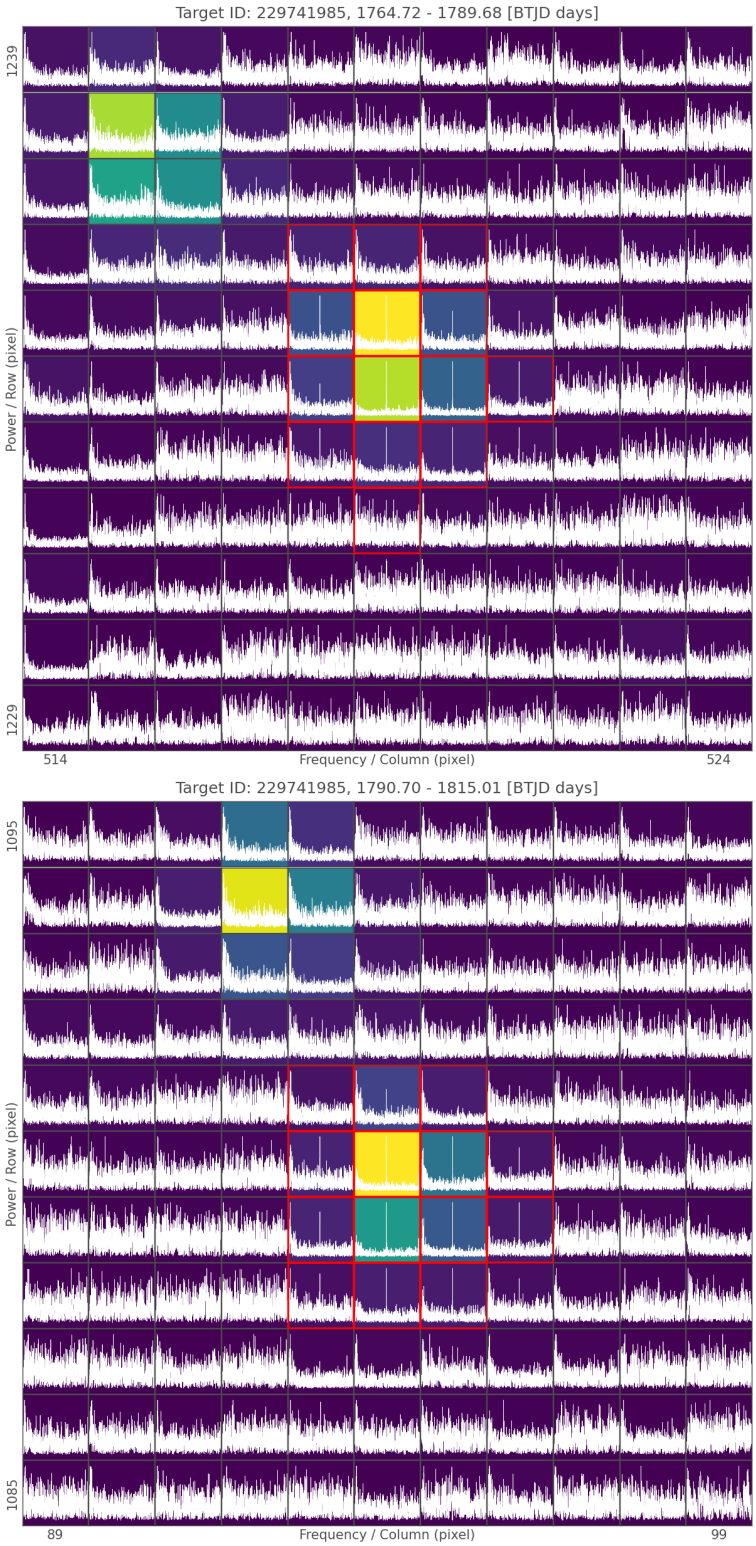

Figure A.11: Pixel map of TIC 229741985 for sector 17 (the first image) and sector 18 (the second image) for the TESS-SPOC pipeline.

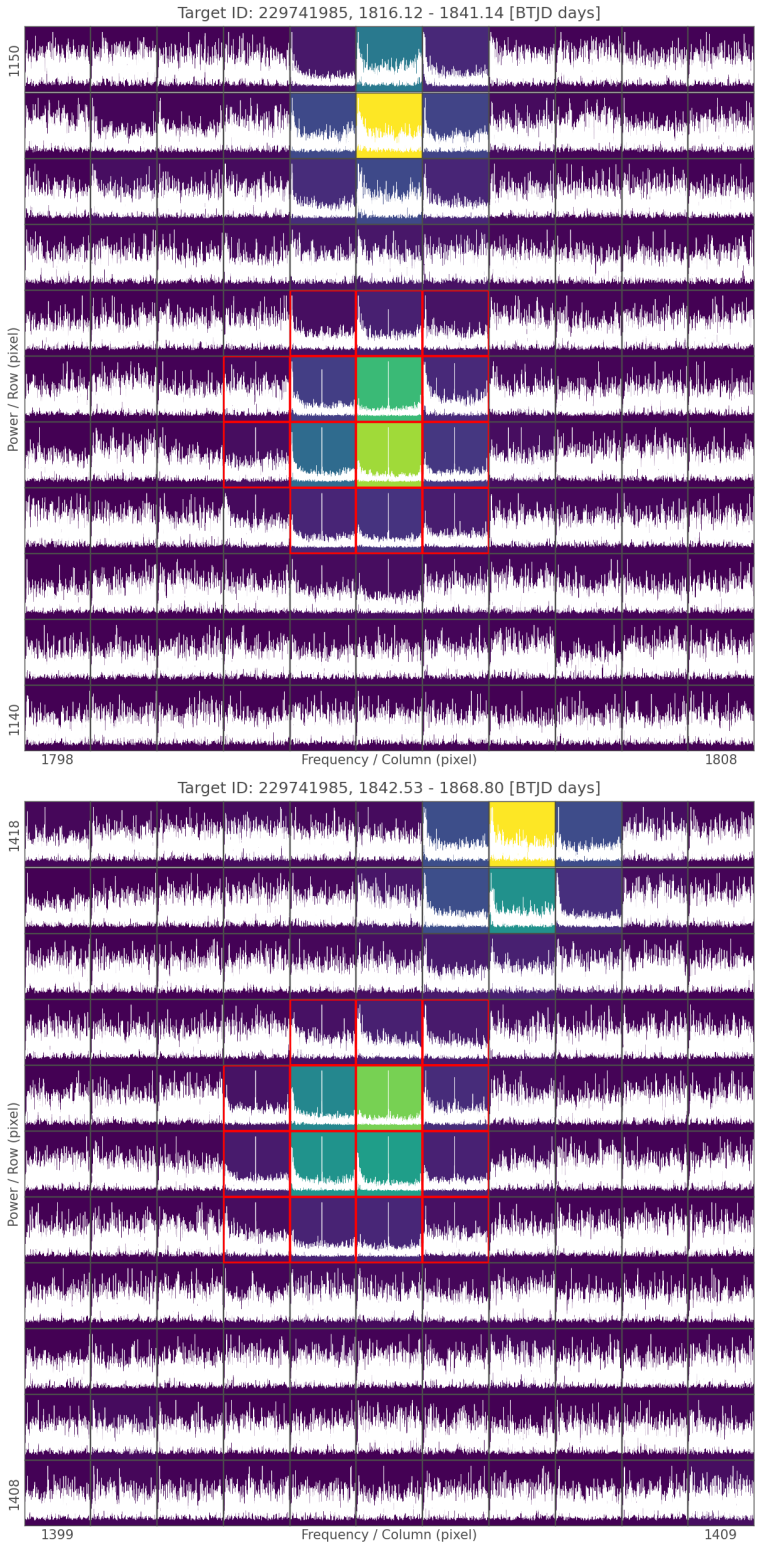

Figure A.12: Pixel map of TIC 229741985 for sector 19 (the first image) and sector 20 (the second image) for the TESS-SPOC pipeline.

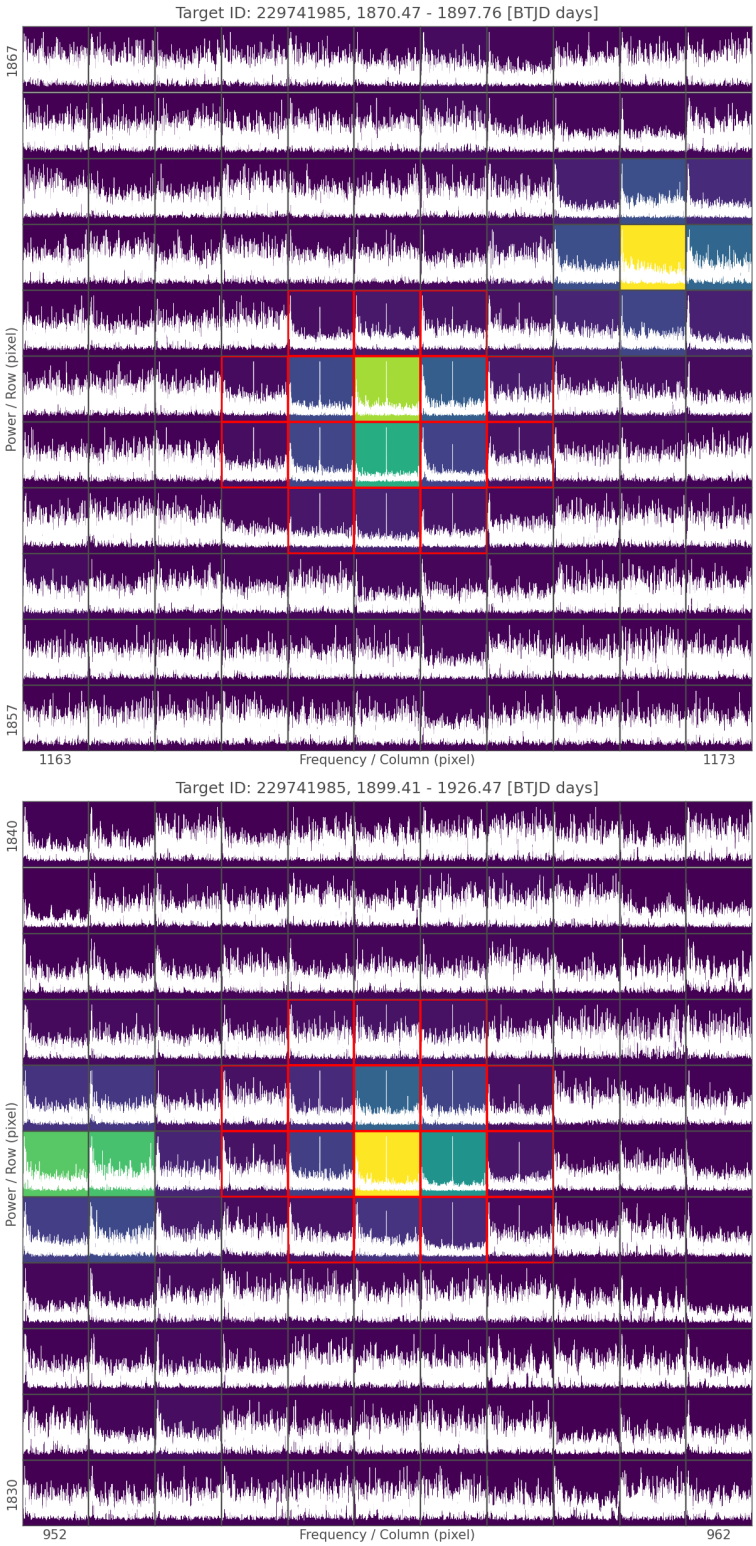

Figure A.13: Pixel map of TIC 229741985 for sector 21 (the first image) and sector 22 (the second image) for the TESS-SPOC pipeline.

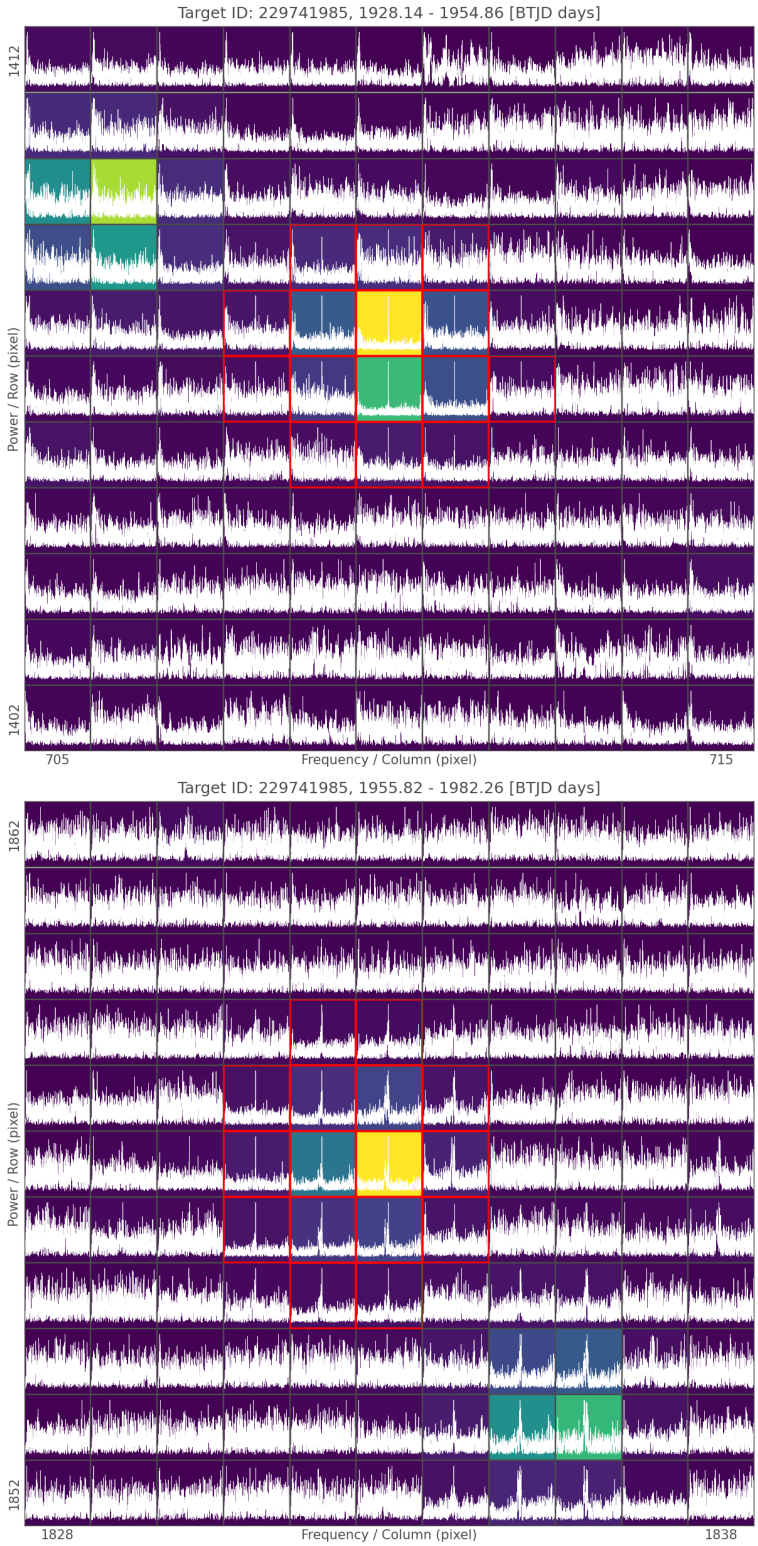

Figure A.14: Pixel map of TIC 229741985 for sector 23 (the first image) and sector 24 (the second image) for the TESS-SPOC pipeline.

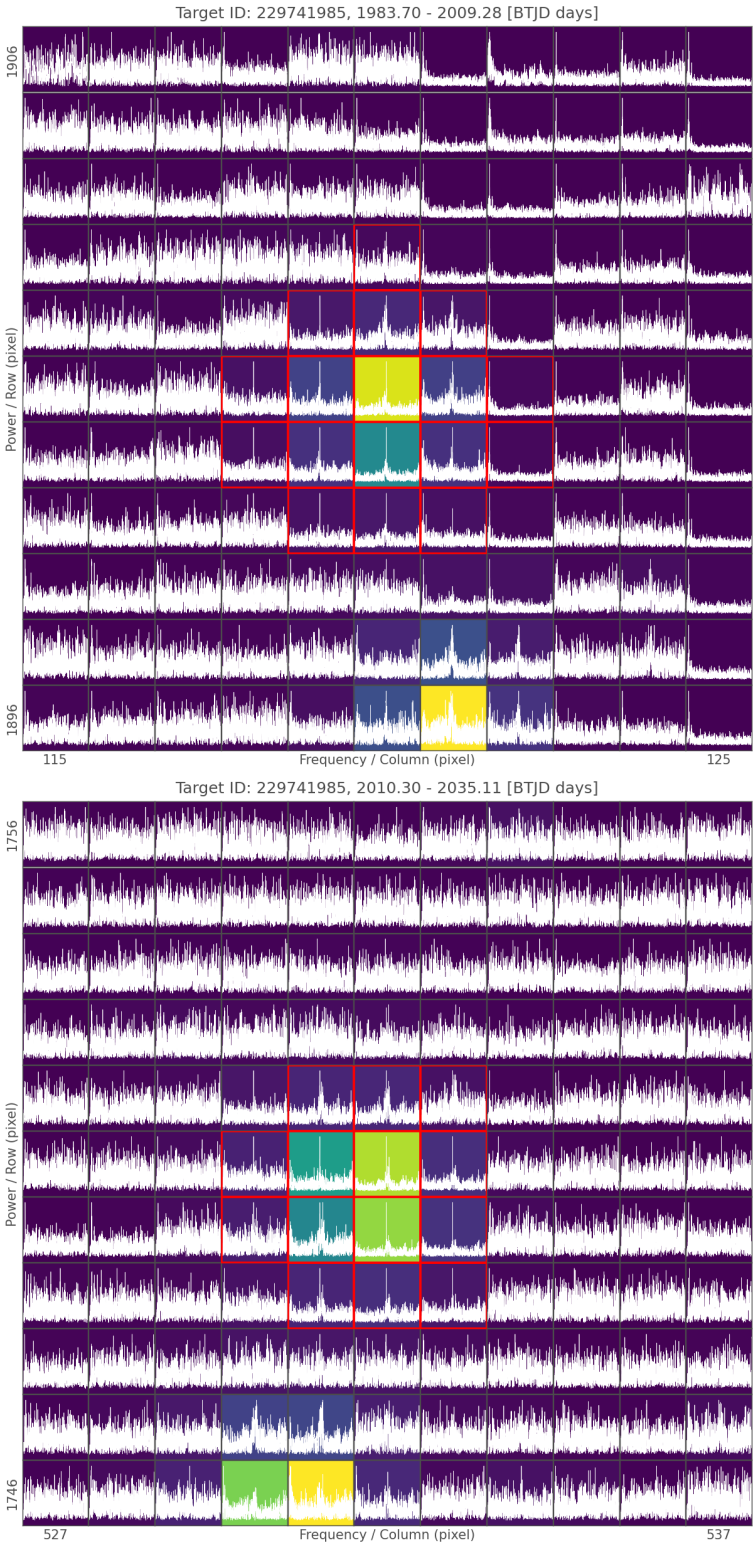

Figure A.15: Pixel map of TIC 229741985 for sector 25 (the first image) and sector 26 (the second image) for the TESS-SPOC pipeline.

Star_number	Source (Gaia DR2)	RA J2000 [°]	DEC J2000 [°]	π [mas]	e_π [mas]	pmRA [mas/yr]	e_pmRA [mas/yr]	pmDE [mas/yr]	e_pmDE [mas/yr]	Gmag [mag]	e_Gmag [mag]	BP-RP [mag]	RV [km/s]	e_RV [km/s]	Teff [K]
1	2265748153772929408	279.7695444	71.34106291	3.2307	0.0203	-10.097	0.038	-11.614	0.034	10.481	0.0002	0.553	-46.89	0.75	6843.67
2	2265747638376850688	279.736211	71.31533147	1.5116	0.0206	6.172	0.039	12.37	0.046	10.9078	0.0004	1.1623	-22.74	0.65	4933.39
3	2265759904803447936	279.7188675	71.35808674							14898	21.001	1.0995			5021.58
4	2265748016333975552	279.7735537	71.32135406	0.751	0.0311	0.511	0.064	1.922	0.059	15.8054	0.0006	1.0432			5068.49
5	2265748188132668160	279.7716086	71.35942266	0.6559	0.0349	4.277	0.065	-7.471	0.071	15.9553	0.0008	0.875			5705.75
6	2265759389407371008	279.6839767	71.33280925	0.4453	0.0332	-3.756	0.064	-0.747	0.066	16.0384	0.0006	0.9223			5650.84
7	2265748016333975168	279.7649714	71.3210173	0.259	0.0385	-4.772	0.076	-3.565	0.071	16.142	0.0007	1.0977			5004
8	2265748153772928000	279.7499778	71.35039221	0.5454	0.0378	-1.358	0.073	-4.502	0.078	16.1839	0.0007	0.8964			5471.75
9	2265747634080046464	279.752891	71.31737577	0.4664	0.0586	-1.028	0.11	-7.06	0.115	16.9865	0.001	1.1913			4923.25
10	2265749661304629120	279.7751919	71.37518486	0.4105	0.0639	-6.465	0.119	-4.067	0.13	17.1954	0.001	0.9463			
11	2265748016333974016	279.7575006	71.32081142	0.4079	0.0854	1.347	0.181	-6.349	0.166	17.5957	0.0014	1.0905			
12	2265759797427439616	279.6992178	71.35131793	0.1989	0.1101	-4.345	0.214	0.703	0.245	17.9006	0.0015	0.7594			
13	2265748183835874560	279.7974035	71.35697353	0.9238	0.1024	-9.133	0.208	-1.315	0.193	17.9823	0.0016	1.8374			

Table A.1: Characteristics of TIC 229741985 and its background stars from Gaia DR2 catalog. RAJ2000 and DEJ2000 are equatorial coordinates for epoch J2000, π is parallax with error, pmRA and pmDE are proper motions in right ascension and declination with errors, and the RV column indicates radial velocities of objects.